Physics – Uspekhi **68** (3) 211 – 231 (2025)

REVIEWS OF TOPICAL PROBLEMS

PACS numbers: **61.46. – w**, **71.35. – y**, **73.21. – b**

Semiconductor nanocrystalline sulfides

S.I. Sadovnikov

DOI: https://doi.org/10.3367/UFNe.2024.08.039732

Contents

Abstract. The paper presents data on phase equilibria in Cu–S, Ag–S, Zn–S, Cd–S, Hg–S, Sn–S, and Pb–S systems and generalizes experimental results on the crystal and electronic structure of twenty polymorphic phases of coarse- and nanocrystalline semiconductor sulfides of copper, silver, zinc, cadmium, mercury, tin, and lead, including information on the band gap width of the sulfides considered. For the first time, using data on the effective masses of charge carriers and dielectric constants, information on the sizes of excitons in coarse-crystalline sulfides is generalized. Allowing for the sizes of excitons, the size effects observed in the electronic (optical) properties of the above sulfides in the nanocrystalline state are considered. It is shown that a decrease in the size of sulfide nanoparticles can be accompanied by a change in the stoichiometry of sulfides as well as their lattice properties.

Keywords: nanocrystalline sulfides, crystal structure, band gap, exciton size, size effects

1. Introduction

Among binary semiconductor compounds, an important place is occupied by such compounds of metals with sulfur as sulfides CuS, Cu_2S, Ag_2S, ZnS, CdS, HgS, SnS, PbS. These sulfides are used in various fields of modern technology. Devices for the conversion and storage of energy (including fuel cells, photoelectrochemical cells for obtaining hydrogen from water, direct converters of solar energy into electricity, and high-capacity batteries and energy storage devices) play an important role in the development of sustainable technologies, solving energy and environmental problems. Sulfides are widely used in micro- and optoelectronics for manufacturing elements of various optical instruments and devices, and in biology and medicine. They are used to create infrared sensors and photodetectors, near and medium infrared lasers, resistance switches, nonvolatile memory devices, ultrasound detectors, thermoelectric converters, and optical switches. These sulfides are used as phosphors for fluorescent devices, light-emitting diodes, and liquid crystal displays, and as photocatalysts, biosensors, and antibacterial drugs. Due to increased interest, the synthesis, structure, and properties of coarse- and nanocrystalline sulfides PbS, ZnS, CdS, Ag_2S, CuS, including colloidal quantum dots, have been analyzed in recent reviews and monographs [1–25]. Coarse-crystalline sulfides of copper and silver are described in monograph [26]; many original publications are devoted to sulfides of copper, mercury, and tin. Particularly noteworthy are the very informative reviews [1, 6], which are rich in references and cover colloidal nanoparticles of not only sulfides, but also selenides and tellurides of various metals, as well as heteronanostructures.

Unfortunately, intensive studies of the synthesis and properties of nanostructured sulfides with different morphologies are usually not accompanied by a detailed study of the crystal structure and do not provide a comprehensive understanding of its possible modification. Conclusions about the structure of nanostructured sulfides are made by visually comparing experimental X-ray diffraction spectra with standard data for the corresponding coarse-crystalline sulfides and comparing the estimated unit cell parameters with the cell parameters of the coarse-crystalline sulfide. However, much data on the crystal structure of coarse-crystalline sulfides was obtained back in the 1950s–1970s and even earlier using samples of natural minerals. Synthesized sulfides are usually purer and do not contain many impurities present in natural samples. This is one of the reasons for the difference between the crystal structures of natural and synthesized sulfides.

The crystal structures of most sulfide phases are quite complex. Therefore, in many experimental studies of the synthesis and properties of sulfide phases, especially nanocrystalline ones, the determination of the crystal structure of the synthesized sulfide is either completely absent [27–30] or is carried out by comparing the experimental results [31–44] of

S.I. Sadovnikov
Institute of Solid State Chemistry,
Ural Branch of the Russian Academy of Sciences,
ul. Pervomaiskaya 91, 620077 Ekaterinburg, Russian Federation
E-mail: sadovnikov@ihim.uran.ru

Received 1 February 2024, revised 3 June 2024
Uspekhi Fizicheskikh Nauk **195** (3) 223 – 244 (2025)
Translated by V L Derbov

X-ray diffraction or transmission electron microscopy (TEM) with outdated diffraction data [45–49], presented in JCPDS cards 14-0072 and 65-2356 for Ag_2S, 19-0798 for HgS, 26-1116 for Cu_2S, 06-0464 for CuS, etc. Thus, in Refs [31, 33, 50, 51], without a full-profile refinement of the structure, it is assumed that the Ag_2S sulfide, synthesized in the form of a film, nanocrystalline powder, or nanoparticles, has the crystal structure of natural acanthite. In the recent paper [52], the structure of Ag_2S quantum dots with an average size of 4.5 nm without a full-profile analysis is described as an outdated monoclinic (space group (sp. gr.) $P2_1/n$) structure of stoichiometric acanthite. The authors of Refs [53–55], devoted to the synthesis of Ag_2S nanoparticles and quantum dots, present X-ray diffraction data without discussing the structure of the synthesized nanocrystalline silver sulfide at all. In Ref. [56], it is assumed that the synthesized silver sulfide film Ag_2S has an argentite structure. However, the crystal structure of synthetic sulfide phases, especially nanocrystalline ones, can have noticeable differences from the structure of natural minerals in terms of the unit cell parameters and even in the arrangement of atoms in other crystallographic positions. This is evidenced, in particular, by the detection of reflections not related to the acanthite-type structure in the diffraction pattern of Ag_2S nanoparticles [50] and the difference in the diffraction reflections in the X-ray patterns of nanostructured CdS from the diffraction reflections of coarse-crystalline cadmium sulfide phases [57–59].

Note that much published experimental diffraction data on sulfide phases is generally not suitable for quantitative determination and refinement of the structure, since they were taken in a narrow range of angles 2θ (usually $20^\circ - 60^\circ$) and without sufficient signal accumulation.

Clarification of the crystal structure of nanocrystalline sulfides is necessary, since only in this way can one detect changes in nonstoichiometric parameters caused by a decrease in the size of sulfide particles. To clarify the structure, one must know the initial values of the current coordinates (xyz) of the compound's atoms. In the original articles, there is usually no information on the atomic coordinates. Such information is available in the Inorganic Crystal Structure Database (ICSD), FIZ Karlsruhe (Germany), but there is no open access to it. Keeping in mind these difficulties, this paper presents information on the atomic coordinates of the sulfides under consideration.

Note that not all substances with particle sizes in the nanometer range from 1 to 100 nm are nanomaterials. In the full sense, nanomaterials are substances in which size effects are manifested, and their properties differ significantly from those of coarse-crystalline substances. In semiconductor compounds, the ratio of particle sizes to exciton size determines whether size effects will be observed in the properties of these substances. In other words, when the size of crystalline particles decreases to sizes comparable to the exciton size, the crystalline substance finds itself in a nanocrystalline state. Therefore, the review includes a brief description of the exciton as a quasiparticle and the definition of the exciton size as a function of the permittivity and effective masses of charge carriers.

2. Phase equilibria and phases of $M-S$ systems with semiconductor sulfides

Phase diagrams of $M-S$ systems (M = Cu, Ag, Zn, Cd, Hg, Sn, Pb) with semiconductor sulfides were constructed mainly in the period of 1985–1996. Intensive studies of the synthesis and properties of nanostructured sulfides carried out during the last 20–25 years affected phase equilibria mainly in the refinement of the boundaries of the homogeneity regions of sulfides. Noticeable changes, especially related to nonstoichiometry, were discovered during careful studies of the structure of nanostructured sulfide phases

2.1 $M-S$ systems of metals in IB group (M = Cu, Ag)

The phase diagram of the Cu–S system in the range from 23 to 55 at.% of S is constructed in Ref. [60]. The main phases of copper sulfide with nonstoichiometry in the copper sublattice are chalcocite Cu_2S ($Cu_{2-x}S$) and hexagonal covellite CuS. Chalcocite has a low-temperature monoclinic (sp. gr. $P2_1/c$) modification α-$Cu_{2-x}S$ (α-$Cu_{1.991-2.002}S$), existing at temperatures below 376.5 K [61, 62]. All atoms of copper Cu and sulfur S in the unit cell of low chalcocite α-$Cu_{2-x}S$ are in crystallographic positions $4(e)$, the filling degree of $4(e)$ positions by Cu atoms is slightly less than 1.0, and the filling degree of $4(e)$ positions of the nonmetallic sublattice by S atoms is 1.0. The unit cell of monoclinic chalcocite α-Cu_2S includes 48 Cu_2S formula units. With increasing temperature, a polymorphic phase transition of low chalcocite α-$Cu_{2-x}S$ into high-temperature high hexagonal (sp. gr. $P6_3/mmc$) chalcocite β-$Cu_{2-x}S$ occurs. The transition temperature, depending on the composition of the low chalcocite, ranges from 263 to 376 K. With increasing temperature, the homogeneity region of the high chalcocite β-$Cu_{2-x}S$ decreases and at a temperature of $T = 473$ K or higher; the high chalcocite has the composition β-$Cu_{1.9994}S$. In the crystal structure of high hexagonal chalcocite β-$Cu_{2-x}S$, Cu atoms statistically (with a probability of less than 1.0) occupy positions $2(b)$, $4(f)$, and $6(g)$ [63] or positions $2(b)$, $4(f)$, and $12(k)$ [48] (Table 1). In the low α-chalcocite, the filling degree of the metallic sublattice sites with Cu atoms is almost equal to 1, whereas, in the high chalcocite β-$Cu_{2-x}S$ at a temperature above 373 K, the filling degree of the metallic sublattice sites with copper atoms is only $\sim 0.1-0.6$ (see Table 1). There is also information about high-temperature face-centered cubic (sp. gr. $Fm\bar{3}m$) chalcocite γ-Cu_2S, which is stable at temperatures above 708–709 K. The simplest structure of γ-Cu_2S may be the antifluorite-type one proposed in Ref. [64]. In this structure, the Cu atoms are located in the $8(c)$ positions, i.e., in the tetrahedral interstices of the sublattice of sulfur atoms occupying the $4(a)$ positions. Later, when studying cubic digenite $Cu_{1.8}S$, it was shown that, in it, two S atoms occupy the $4(a)$ positions, and 7.2 Cu atoms are statistically located at the $192(l)$ [65] or $4(b)$, $8(c)$, and $192(l)$ positions with occupation probabilities of ~ 0.25, ~ 0.05, and ~ 0.026 [66], respectively. In subsequent theoretical papers [67, 68], taking into account the studies [65, 66] of cubic digenite $Cu_{1.8}S$, it was accepted that the unit cell of cubic (sp. gr. $Fm\bar{3}m$) chalcocite γ-Cu_2S is similar to the unit cell of digenite $Cu_{1.8}S$ and includes four formula units of Cu_2S. In the unit cell of cubic chalcocite γ-Cu_2S, which has a period $a \approx 0.564-0.576$ nm at a temperature of ~ 770 K [50], two S atoms occupy positions $4(a)$, while eight Cu atoms are statistically located at positions $4(b)$, $8(c)$, and $192(l)$ with occupation probabilities of $\sim 0.03-0.09$, $\sim 0.25-0.26$, and $\sim 0.030-0.035$, respectively. However, the structure of cubic chalcocite γ-Cu_2S has not been definitively established. The authors of Ref. [69] determined that the temperature of the β-Cu_2S–γ-Cu_2S transition is 710 K.

Table 1. Crystal structures of high hexagonal (sp. gr. No. 194 — $P6_3/mmc$ (D_{6h}^4)) chalcocite β-Cu_2S [48, 63] and hexagonal (sp. gr. No. 194 — $P6_3/mmc$ (D_{6h}^4)) covellite CuS [73].

Phase, structure type, space group	Lattice parameters, nm	Atom	Position and multiplicity	Atomic coordinates			Filling degree
				x/a	y/b	z/c	
High hexagonal chalcocite β-Cu_2S [63], $P6_3/mmc$ (D_{6h}^4)	$a = 0.395$ $c = 0.675$	Cu1	2(b)	0	0	1/4	0.870
		Cu2	4(f)	1/3	2/3	0.568	0.345
		Cu3	6(g)	0	1/2	0	0.140
		S1	2(d)	2/3	1/3	1/4	1.0
High hexagonal chalcocite β-Cu_2S [48], $P6_3/mmc$ (D_{6h}^4)	$a = 0.3961$ $c = 0.6722$	Cu1	2(b)	0	0	1/4	0.60
		Cu2	4(f)	1/3	2/3	0.40	0.10
		Cu3	12(k)	0.2165	0.4330	0.43	0.13
		Cu4	12(k)	0.1665	0.5830	0.467	0.07
		S1	2(d)	1/3	2/3	3/4	1.0
Hexagonal covellite CuS [73], $P6_3/mmc$ (D_{6h}^4)	$a = 0.37938$ $c = 1.6341$	Cu1	2(d)	2/3	1/3	1/4	1
		Cu2	4(f)	1/3	2/3	0.1073	1
		S1	2(c)	1/3	2/3	1/4	1
		S2	4(e)	0	0	0.0634	1

In the literature, the notations of low monoclinic and cubic chalcocite are often confused. For example, in Ref. [70], low monoclinic chalcocite is denoted as γ-Cu_2S, and cubic chalcocite, as α-Cu_2S.

The unit cells of low α-Cu_2S, high β-Cu_2S, and cubic γ-Cu_2S chalcocite are shown in Fig. 1.

The low (significantly less than 1) filling degree of the metallic sublattice positions in all polymorphic chalcocite modifications means that the Cu atoms (ions) in the Cu_2S ($Cu_{2-x}S$) phases are highly disordered, behave like a 'liquid,' and possess high mobility, ensuring the superionic conductivity of these phases [70–72].

The crystal structure of hexagonal (sp. gr. $P6_3/mmc$) covellite CuS [73] is described in Table 1. The unit cell of covellite includes six formula units of CuS. The unit cell parameters of covellite CuS are $a = 0.37917$ nm, $c = 1.6342$ nm [74], or $a = 0.3792$ nm, $c = 1.6344$ nm [75] and are close to those given in Table 1. Unlike chalcocite, covellite CuS is a stoichiometric compound, contains 50 at.% of S, and has virtually no homogeneity region. Covellite demonstrates peritectic decomposition into digenite $Cu_{9-x}S_5$ and sulfur S at $\sim$ 780 K.

In addition to α- and β-chalcocite $Cu_{2-x}S$ and covellite CuS, in the Cu–S system there are compounds such as djurleite $Cu_{1.96}S$, anilite Cu_7S_4 ($Cu_{1.75}S$), and digenite $Cu_{9-x}S_5$, which have polymorphic modifications, as well as several metastable phases.

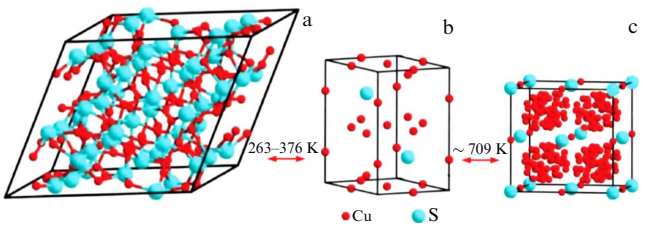

Figure 1. Changes in crystal structure of chalcocite Cu_2S during reversible phase transformations. Shown are unit cells of (a) low monoclinic (sp. gr. $P2_1/c$) chalcocite α-$Cu_{2-x}S$, (b) high hexagonal (sp. gr. $P6_3/mmc$) chalcocite β-$Cu_{2-x}S$, and (c) cubic chalcocite γ-Cu_2S, constructed by the author of the review based on data from Refs [63, 73]. For chalcocite γ-Cu_2S, positions of metallic sublattice are shown in which Cu atoms can be located with a probability of less than $\sim$ 0.1.

The phase diagram of the Ag–S system [13, 76] includes three main polymorphic modifications of silver sulfide Ag_2S (Fig. 2). The low-temperature semiconductor phase α-Ag_2S with a monoclinic structure (acanthite) exists at temperatures below $\sim$ 450 K. The cubic phase β-Ag_2S (argentite) under equilibrium conditions exists in the temperature range of 452–859 K, has a body-centered cubic (BCC) sublattice of sulfur atoms, and possesses superionic conductivity. The high-temperature cubic phase γ-Ag_2S with a face-centered cubic (FCC) sublattice of sulfur atoms is stable at temperatures from $\sim$ 860 K to the melting point.

In the literature, the notations of monoclinic acanthite and cubic argentite are often confused. For example, in Refs [45, 77–80], the monoclinic phase (acanthite) is denoted as β-Ag_2S, and the BCC phase (argentite) is denoted as α-Ag_2S.

The parameters of the crystal lattices of the phases α-Ag_2S, β-Ag_2S, and γ-Ag_2S and the coordinates of the Ag and S atoms in them are presented in Table 2.

Usually the monoclinic α-Ag_2S phase is considered stoichiometric, whereas the cubic β-$Ag_{2\pm\delta}S$ and γ-$Ag_{2\pm\delta}S$ phases with $\delta \cong 0.002$ are nonstoichiometric and can exhibit both a slight deficit and a slight excess of silver. The homogeneity regions of the cubic allotropic forms of silver sulfide Ag_2S are determined in Refs [79, 81–84].

Determination of the crystal structure in a single crystal of the natural mineral acanthite [45] showed that the unit cell of acanthite α-Ag_2S is primitive monoclinic and belongs to the space group $P2_1/n$ ($P12_1/n1$). Later, the authors of Ref. [85] showed that the structure of monoclinic acanthite α-Ag_2S is more accurately described in the space group $P2_1/c$ ($P12_1/c1$). The axes $\mathbf{a}_{P2_1/c}$ and $\mathbf{b}_{P2_1/c}$ of the unit cell [85] coincide in magnitude and direction with the axes $\mathbf{a}_{P2_1/n}$ and $\mathbf{b}_{P2_1/n}$ of the unit cell [45], and the axis $\mathbf{c}_{P2_1/c} = (\mathbf{c}_{P2_1/n} - \mathbf{a}_{P2_1/n})$. The crystal structure of the synthesized coarse-crystalline silver sulfide was refined in Ref. [86], according to which the low-temperature phase of silver sulfide has a monoclinic (sp. gr. $P2_1/c$) structure of the α-Ag_2S acanthite type and does not contain vacancies, i.e., the coarse-crystalline acanthite is stoichiometric (see Table 2).

According to Ref. [87], the unit cell of argentite β-Ag_2S has a cubic (sp. gr. $Im\bar{3}m$ ($I4/m\bar{3}2/m$) (O_h^9)) structure and includes two Ag_2S formula units. Two sulfur atoms S

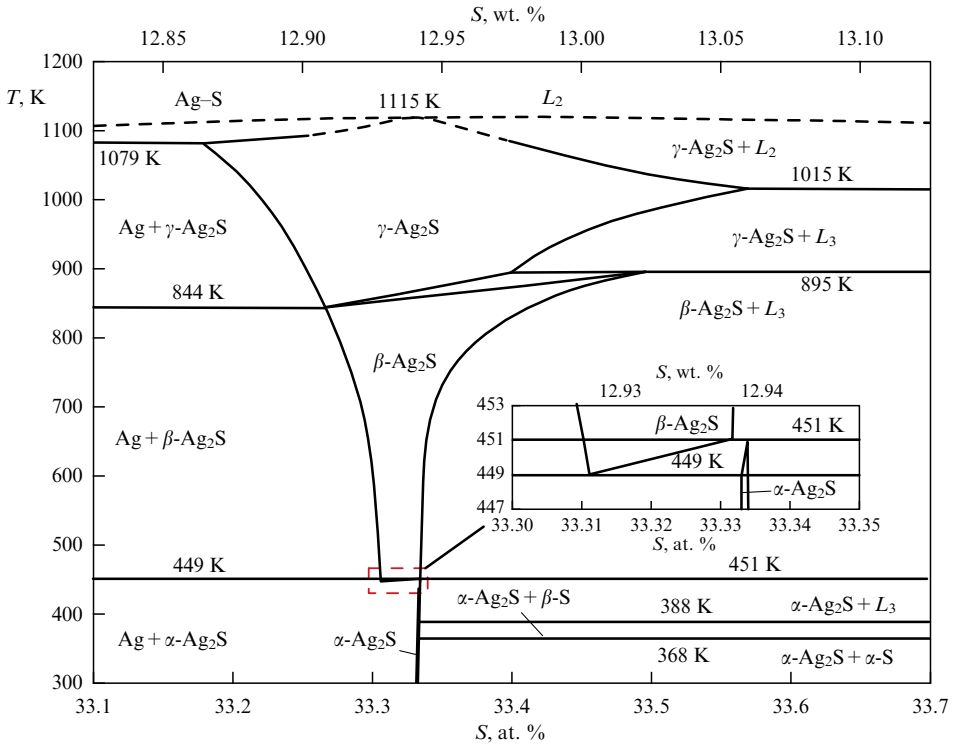

Figure 2. Phase diagram of Ag – S system in vicinity of silver sulfide Ag_2S, constructed by the author of the review based on data from Refs [13, 76]. Inset shows phase equilibria of α-Ag_2S–β-Ag_2S near temperature of 450 K.

Table 2. Crystal structures of coarse-crystalline low-temperature monoclinic acanthite α-Ag_2S at 298 K [86], body-centered cubic argentite β-Ag_2S at 503 K [90], and high-temperature face-centered cubic phase γ-Ag_2S of silver sulfide at ~ 923 K [89].

Phase, structure type, space group	Lattice parameters, nm	Atom	Position and multiplicity	Atomic coordinates			Filling degree
				x/a	y/b	z/c	
Monoclinic acanthite α-Ag_2S, $P2_1/c$ (C_{2h}^5)	$a = 0.42264$ $b = 0.69282$ $c = 0.95317$ $\beta = 125.55°$	Ag1 Ag2 S	4(e) 4(e) 4(e)	0.0715 0.7264 0.492	1.00 1.00 1.00	0.3094 0.4375 0.1321	1.00 1.00 1.00
Cubic argentite β-Ag_2S, $Im\bar{3}m$ (O_h^9)	$a = 0.4874$	Ag1 Ag2 S	6(b) 48(j) 2(a)	0 0 0	0.5 0.3306 0	0.5 0.4122 0	0.0978 0.0711 1.0
Cubic phase γ-Ag_2S, $Fm\bar{3}m$ (O_h^5)	$a = 0.62831$	Ag1 Ag2 Ag3 S	8(c) 32(f) 48(i) 4(a)	0.25 0.3034 0.5 0	0.25 0.3034 0.3814 0	0.25 0.3034 0.3814 0	0.088 0.150 0.027 1

occupy crystallographic positions 2(a) and form a BCC sublattice. Four silver atoms Ag are statistically distributed with equal probability among 42 positions 6(b), 12(d), and 24(h).

Neutron diffraction study [88] of artificial crystal of argentite β-Ag_2S in the temperature range of 459–598 K confirmed the cubic (sp. gr. $Im\bar{3}m$) structure of this phase but significantly clarified the distribution of Ag atoms. According to Ref. [88], four Ag atoms are statistically distributed over 18 positions 6(b) and 12(d). The probabilities of filling positions 6(b) and 12(d) depend on the temperature.

According to high-temperature X-ray data [89], in contrast to [88], in argentite β-Ag_2S, four Ag atoms are statistically distributed over 54 positions 6(b) and 48(j) with occupation probabilities of ~ 0.097 and ~ 0.0715, respectively.

The latest refinements of the crystal structure of the synthesized coarse-crystalline argentite β-Ag_2S were carried out in Ref. [90]. According to these data, in cubic (sp. gr. $Im\bar{3}m$) argentite β-Ag_2S at a temperature of ~ 460 K, a deviation from stoichiometry in silver content is observed.

A model for the structure of the high-temperature cubic (sp. gr. $Fm\bar{3}m$) phase in γ-Ag_2S silver sulfide was proposed in Ref. [91]: four S atoms occupy crystallographic positions 4(a) and form an FCC sublattice, and eight Ag atoms are statistically distributed over positions 8(c) and 32(f). The authors of Ref. [89], using high-temperature X-ray data, refined model [91] by placing Ag atoms also at positions 48(i). According to Ref. [90], a noticeable silver deficiency is

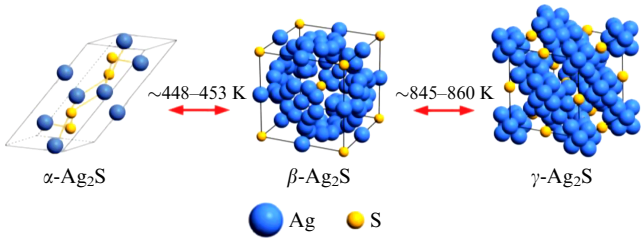

Figure 3. Changes in crystal structure of silver sulfide during reversible phase transformations. Shown are unit cells of monoclinic (sp. gr. $P2_1/c$) acanthite α-Ag_2S, cubic (sp. gr. $Im\bar{3}m$) argentite β-Ag_2S, and cubic (sp. gr. $Fm\bar{3}m$) phase γ-Ag_2S. In unit cells of β-Ag_2S and γ-Ag_2S, positions of metallic sublattice are marked in which Ag atoms can be located with a probability of less than ~ 0.1. (Reproduced from [92] with permission from Springer.)

observed in the cubic γ-phase, corresponding to nonstoichiometric sulfide $Ag_{1.7}S$ (see Table 2).

The unit cells of monoclinic acanthite α-Ag_2S, BCC argentite β-Ag_2S, and high-temperature FCC phase γ-Ag_2S are shown in Fig. 3.

The presence of vacancies in the metallic sublattice of nanocrystalline silver sulfide was experimentally established by one of the methods of electron-positron annihilation that implies measuring the lifetime of positrons [93].

Low degrees of filling the positions of the metallic sublattice of cubic phases β-Ag_2S and γ-Ag_2S mean, as in the case of copper sulfides $Cu_{2-x}S$, that atoms (ions) of silver in phases β-Ag_2S and γ-Ag_2S are strongly disordered. Indeed, the number of Ag atoms in cubic phases β-Ag_2S and γ-Ag_2S is much less than the number of sites in the metallic sublattice; therefore, significant positional disorder in the distribution of Ag and a huge (more than 92%) concentration of vacant sites facilitate jumps of silver cations and provide superionic conductivity of these phases. In the general case, the metallic sublattice of β-Ag_2S argentite can be considered an anisotropic strongly interacting Coulomb liquid of Ag^+ cations which diffuse under the action of an effective potential of BCC anionic sulfur lattice.

In addition, in cubic argentite, the possible distances between silver atoms are too small for the 6(*b*) and 48(*j*) positions to be occupied by Ag atoms with a probability equal to unity. Therefore, the degrees of filling the 6(*b*) and 48(*j*) positions by Ag atoms (i.e., the probability of detecting Ag atoms in the 6(*b*) and 48(*j*) positions) are very small (less than 0.1: see Table 2). Physically, this means that, in the cubic argentite lattice, four silver atoms are in continuous motion over 54 possible crystallographic positions. It is precisely this continuous motion of the Ag^+ cations that ensures the stability of the cubic argentite crystal lattice and its superionic conductivity. The diffusion of silver atoms in argentite occurs via a vacancy mechanism, when an Ag atom (ion) jumps to a neighboring unoccupied site.

2.2 *M*–S systems of metals in IIB group (*M* = Zn, Cd, Hg)

The only compound of the Zn–S system is zinc sulfide, which contains 50 at.% of S, exists in two polymorphic modifications, and has a melting point of ~ 1991 K [94].

The low-temperature cubic (sp. gr. $F\bar{4}3m$ (T_d^2)) modification of α-ZnS has the cubic structure of zinc blende, or sphalerite, ZnS (type *B*3) and is stable at temperatures below 1290 K. At 1293 K, the low-temperature cubic zinc sulfide

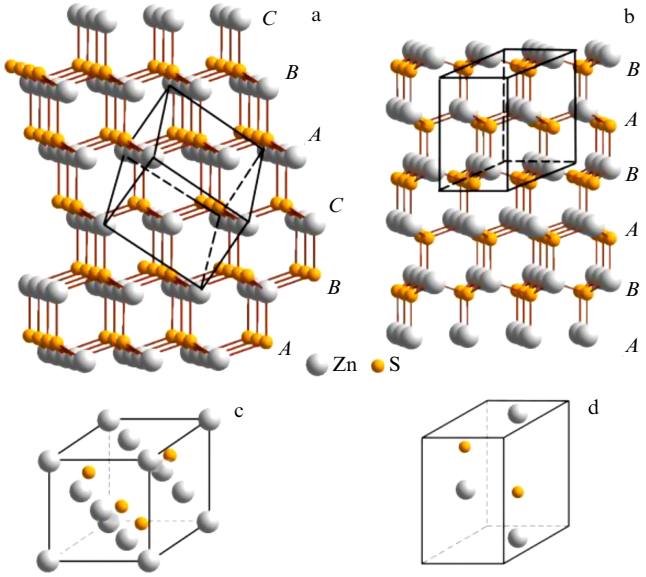

Figure 4. Sequences of alternating close-packed layers of Zn and S atoms for (a) α-ZnS with *B*3 structure and (b) β-ZnS with *B*4 structure with contours of unit cells shown. Unit cells of zinc sulfides: (c) low-temperature cubic (sp. gr. $F\bar{4}3m$) α-ZnS (*B*3 structure (zinc blende or sphalerite)), (d) high-temperature hexagonal (sp. gr. $P6_3mc$) β-ZnS (*B*4-type structure (wurtzite)). (Figure constructed by the author of the review based on data from [46, 47].)

transforms into the high-temperature hexagonal (sp. gr. $P6_3mc$ (C_{6v}^4)) modification of β-ZnS with a wurtzite structure (type *B*4) [94], which retains semiconductor properties.

At a temperature of 300 K, cubic α-ZnS with a sphalerite structure has a lattice period of $a = 0.54109$ nm [46]. According to X-ray data, the unit cell of hexagonal wurtzite β-ZnS has parameters $a = 0.38230$ and $c = 0.62565$ nm [47], while, according to neutron diffraction data [95], its parameters are somewhat different. There is also information [47, 96–98] on the face-centered cubic (sp. gr. $Fm\bar{3}m$) phase of γ-ZnS, formed at a temperature of ~ 1000 K and a pressure of ~ 27–35 GPa.

Low-temperature cubic α-ZnS and high-temperature hexagonal β-ZnS modifications of coarse-crystalline zinc sulfide differ in the sequence of alternating close-packed layers of atoms (ions) of different types, displaced relative to each other.

The *B*3 structure of zinc sulfide α-ZnS (zinc blende or sphalerite) is a cubic closest packing (Fig. 4a), in which the close-packed layers are located perpendicular to the $[111]_{B3}$ direction (or equivalent directions). The *B*4 structure of zinc sulfide β-ZnS (wurtzite type) has a hexagonal close packing, in which the close-packed layers are located perpendicular to the *z*-axis, the $[001]_{B4}$ direction (Fig. 4b). In the ideal wurtzite-type structure, the lattice basis contains two metal atoms in the 2(*b*) positions with coordinates (1/3 2/3 0) and (2/3 1/3 1/2) and two nonmetal atoms in the 2(*b*) positions with coordinates (1/3 2/3 3/8) and (2/3 1/3 7/8). In the real β-ZnS structure, the sulfur atoms are slightly shifted along the *z* coordinate. The unit cells of cubic α-ZnS and hexagonal β-ZnS zinc sulfides are shown in Fig. 4c and 4d, respectively.

In Ref. [99], a nanocrystalline ZnS powder with a particle size of ~ 5 nm was obtained. According to [99], the ZnS nanopowder has the same disordered hexagonal structure with random (nonperiodic) alternation of close-packed atomic planes as that previously discovered in nanocrystal-

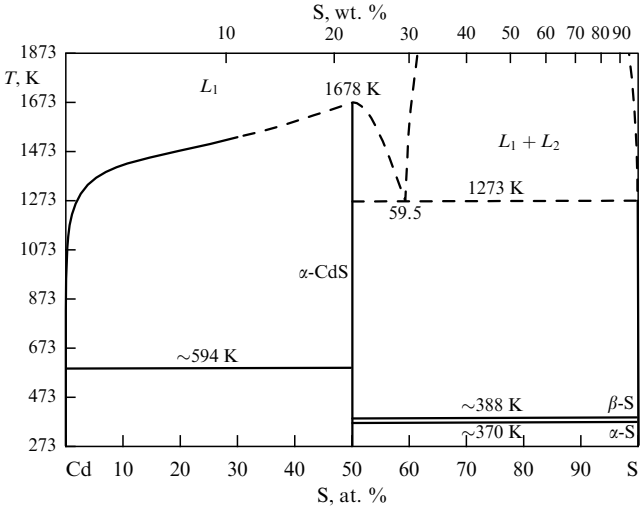

Figure 5. Phase diagram of Cd–S system. (Figure constructed by the author of the review based on data from [13, 101].)

line cadmium sulfide CdS [100]. The periods of the unit cell of the ZnS nanopowder with an average hexagonal lattice are $a = 0.216$ nm and $c = 0.306$ nm. In Ref. [99], there is no information on the refinement of the structure of the ZnS nanopowder; therefore, its results on the structure, obtained by analogy with the previous study [100], are not entirely reliable.

The cubic sphalerite type and hexagonal wurtzite type crystal structures are typical not only of zinc sulfide, but also of cadmium and mercury sulfides, as well as of a number of selenides, arsenides, and tellurides.

Cadmium sulfide CuS is the only compound existing in the Cd–S system (Fig. 5). Cadmium sulfide contains 50 at.% of S and has a melting point of 1678 K [13, 101]. According to Ref. [102], the melting point of CdS at a pressure of 10.5 atm is 1748 ± 15 K. At atmospheric pressure, sublimation of CdS begins at 1253 K. Coarse-crystalline cadmium sulfide has a low-temperature cubic (sp. gr. $F\bar{4}3m$) β-CdS and a high-temperature hexagonal (sp. gr. $P6_3mc$) α-CdS modification, identified as zinc blende (sphalerite) structures of ZnS (type *B*3) and wurtzite ZnS (type *B*4), respectively [103].

The unit cell parameters of cubic β-CdS and hexagonal α-CdS are presented in [104, 105], respectively. At a pressure of 27 kbar, a phase transition from the hexagonal (sp. gr. $P6_3mc$) structure *B*4 to the cubic (sp. gr. $Fm\bar{3}m$) structure *B*1 is observed in CdS, while cadmium sulfide retains its semiconductor properties [106].

Experimental studies of CdS films with thicknesses from 6 to 70 nm, synthesized using various methods [107–109], nanoparticles [110, 111], and complex forms of nanostructured CdS, indicate that their structures do not correspond to those of coarse-crystalline CdS wurtzite or sphalerite modifications. The authors of Refs [58, 100] found that CdS nanoparticles have a specific disordered hexagonal structure with random (nonperiodic) alternation of close-packed atomic planes. The authors of Ref. [57] analyzed the structure of nanocrystalline sulfides, which in the normal state have *B*3 and *B*4 structures. They showed that, in sulfide nanoparticles with a small number of closely packed atomic planes, the principle of a regular sequence of packings is not observed and, consequently, there is no crystalline periodicity in them [57]. This means that, in nanosized crystals, a

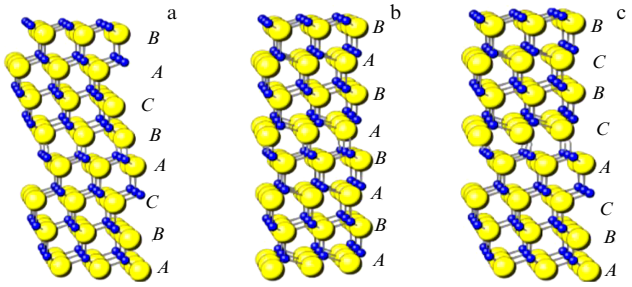

Figure 6. Alternation of close-packed planes in ordered and disordered phases of cadmium sulfide CdS: (a) cubic sphalerite *B*4 structure; (b) hexagonal wurtzite *B*3 structure; (c) disordered structure. (Reproduced from [57] with permission of JUCr Journals.)

disordered structure is more important than a periodic arrangement of packing layers.

The authors of Ref. [57] considered the nonperiodic structure of sulfide nanoparticles using cadmium sulfide CdS as an example. The explanation of the nanostructured cadmium sulfide CdS structure is based on the principle of closest packing, common to *B*3 and *B*4 structures, since these structures contain alternating close-packed planes consisting of either cadmium or sulfur atoms. The superposition of the planes is carried out in such a way that all cadmium atoms are in a tetrahedral environment of sulfur atoms, and all sulfur atoms are in a tetrahedral environment of cadmium atoms. The difference among the *B*3, *B*4, and polytype structures consists only in the sequence of alternating close-packed planes. Thus, in a cubic structure of type *B*4, the closest packing $ABC\ldots$ is realized, in a hexagonal structure of type *B*3, the closest packing $AB\ldots$ is realized, and in a disordered CdS structure, the planes alternate randomly (Fig. 6).

To calculate the positions of the peaks in the X-ray diffraction pattern of such a disordered structure, the authors of Refs [57–59, 100] examined its average crystal lattice. This lattice has hexagonal (sp. gr. *P*6) symmetry and is described by a unit cell with parameters $a = a_0/\sqrt{3} = 0.238$ nm and $c = 0.337$ nm (a_0 is the distance between like atoms in a plane, c is the distance between the nearest close-packed planes of cadmium or sulfur in an ordered CuS crystal). The unit cell of disordered CdS contains a Cd atom with coordinates (000) and an S atom with coordinates $(0\,0\,1/\sqrt{24})$; the filling degree of all atomic positions is 1/3 (Table 3).

Table 3. Model hexagonal (sp. gr. no. 168 — *P*6 (C_6^1)) disordered close-packed structure of CdS nanoparticles with a size of 3–9 nm with 'average' lattice at 298 K [13, 59]; $a = 0.236$ nm, $c = 0.334$ nm.

Atom	Position and multiplicity	Atomic coordinates			Filling degree
		x/a	y/a	z/c	
Cd	1(*a*)	0	0	0	1/3
S	1(*a*)	0	0	$1/\sqrt{24} \approx 0.204$	1/3

In Fig. 7, the position of the peaks in the line spectrum from the disordered structure of cadmium sulfide with the *P*6 space group is compared with the experimental spectrum (Fig. 7a) of nanostructured cadmium sulfide obtained in Refs [58, 59, 100]. The experimental spectrum has features characteristic of the spectra of CdS thin films and nanopowders. The large width of the peaks in the experimental X-ray

Table 4. Crystal structures of α-HgS and β-HgS phases [113] of mercury sulfide.

Phase, structure type, space group	Lattice parameters, nm	Atom	Position and multiplicity	Atomic coordinates			Filling degree
				x/a	y/b	z/c	
Trigonal phase α-HgS, $P3_121$ (D_3^4)	$a = 0.41488$ $c = 0.95039$	Hg S	3(*a*) 3(*b*)	0.280 0.508	0 0	0.3333 0.8333	1.0 1.0
Cubic phase β-HgS, type *B*3 (α-ZnS), $F\bar{4}3m$ (T_d^2)	$a = 0.58514$	Hg S	4(*a*) 4(*c*)	0 0.25	0 0.25	0 0.25	1.0 1.0

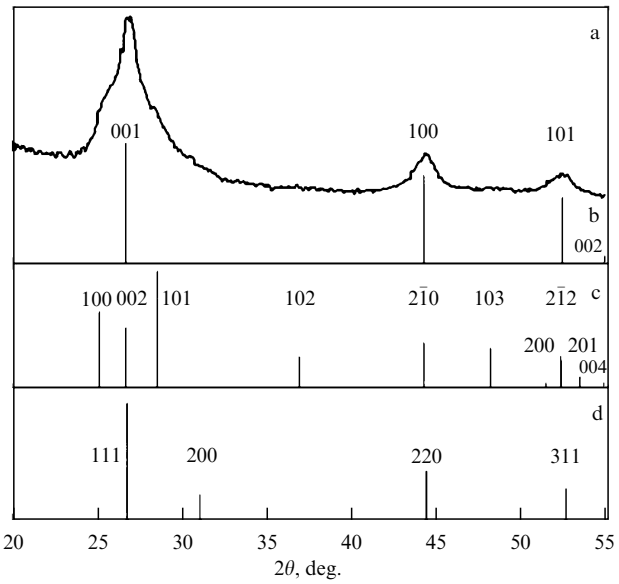

Figure 7. Comparison of experimental X-ray diffraction pattern of (a) CdS nanopowder with calculated line spectra; (b) disordered structure with an 'average' hexagonal (sp. gr. *P*6) lattice; (c) hexagonal (sp. gr. $P6_3mc$) wurtzite type structure *B*3; (d) cubic (sp. gr. $F\bar{4}3m$) sphalerite structure *B*4. (Figure constructed by the author of the review based on data from [57–59, 100].)

diffraction pattern of CdS (Fig. 7a) is due to the small size of the coherent scattering regions (CSRs) in the nanostructured CdS sample. The periods of the unit cell of CdS with an average hexagonal lattice, taken for the model calculation, are $a = 0.236$ nm and $c = 0.334$ nm.

As can be seen, the positions and relative intensities of the diffraction reflections in the spectrum calculated for the average lattice (Fig. 7b) are in good agreement with the experimental data. The calculated line spectra of cadmium sulfide with wurtzite (Fig. 7c) and sphalerite (Fig. 7d) structures differ significantly from the experimental X-ray diffraction pattern.

In general, nonempirical calculations of X-ray diffraction patterns of CdS powders in Refs [57–59, 100] and comparison with experimental spectra showed that the atomic structure of cadmium sulfide nanoparticles with a size of less than 5 nm is disordered.

Mercury sulfide HgS is the only compound in the Hg–S system. Mercury sulfide contains ~ 50 at.% of S and has a melting point of ~ 1093 K [112]. Mercury sulfide has three polymorphic modifications.

The low-temperature trigonal (sp. gr. $P3_121$ (D_3^4)) modification α-HgS (cinnabar) is stable at temperatures below ~ 607–618 K [113]. In the temperature range of ~ 618–754 K, there is a cubic (sp. gr. $F\bar{4}3m$ (T_d^2)) modification β-HgS (metacinnabar) with a *B*3 structure (sphalerite α-ZnS). The high-temperature hexagonal phase γ-HgS (hypercinnabar) with lattice parameters $a = 0.7010$ nm and $c = 1.4130$ nm or $a = 0.6860$ nm and $c = 1.4070$ nm, stable from ~ 745–754 K to the melting point of ~ 1093 K, was discovered in synthesized and natural samples of mercury sulfide [112]. In the same paper, a section of the phase diagram of the Hg–S system was constructed in the region of existence of three modifications of mercury sulfide. According to the data from Ref. [112], the hexagonal phase γ-HgS is defective in the metallic sublattice, and the unit cell of this phase includes 12 formula units of HgS. Traces of the γ-HgS phase were also discovered in Ref. [114]. According to Ref. [115], weak reflections appear in the X-ray diffraction pattern of mercury sulfide at a temperature of 798 K, indicating a phase transition β-HgS–γ-HgS. Presumably, the structure of γ-HgS is described in the space group $P6/mmm$. In none of the above papers were the atomic coordinates determined in the structure of the γ-HgS hexagonal phase.

The parameters of the unit cells of α-HgS and β-HgS and the coordinates of the Hg and S atoms in them are given in Table 4.

2.3 *M*–S systems of metals in IVA group (*M* = Sn, Pb)

In the Sn–S system, there are three stable compounds, SnS, Sn_2S_3, SnS_2, and the metastable phase Sn_3S_4. Tin sulfides SnS and SnS_2 have two polymorphic modifications each, and the sulfide Sn_2S_3 has four polymorphic modifications α, β, γ, and δ [119]. A part of the phase diagram for the Sn–S system in the region of existence of tin sulfides is shown in Fig. 8.

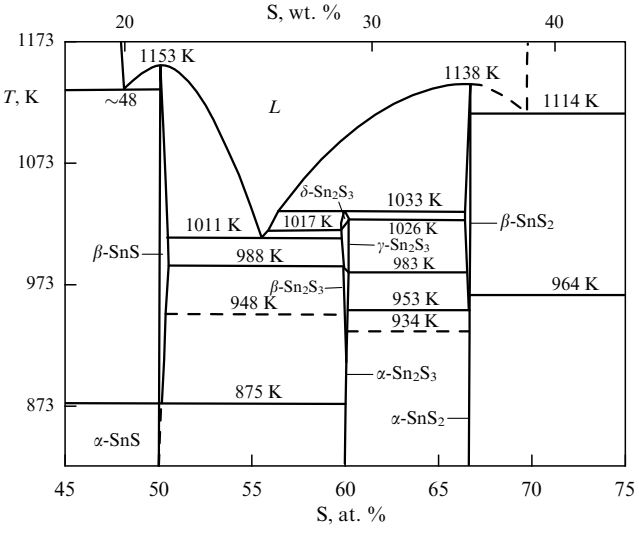

Figure 8. Phase diagram of Sn–S system in region from 45 to 70 at.% S, where tin sulfide phases are observed. (Figure constructed by the author of the review based on data from Refs [116, 119, 121].)

Table 5. Crystal structures of coarse-crystalline orthorhombic low-temperature α-SnS phase [119] and high-temperature β-SnS phase of tin sulfide at 298 K [121].

Phase, structure type, space group	Lattice parameters, nm	Atom	Position and multiplicity	Atomic coordinates			Filling degree
				x/a	y/b	z/c	
Orthorhombic α-SnS, *Pnma* (*Pbnm*) (D_{2h}^{16})	$a = 1.1200$ $b = 0.3987$ $c = 0.4334$	Sn S	4(*c*) 4(*c*)	0.1194 0.3508	0.25 0.25	0.1198 0.0207	1.0 1.0
Orthorhombic β-SnS, *Cmcm* (D_{2h}^{17})	$a = 1.1481$ $b = 0.4177$ $c = 0.4148$	Sn S	4(*c*) 4(*c*)	0 0	0.120 0.349	0.25 0.25	1.0 1.0

Tin monosulfide SnS contains ~ 50 at.% of S and has a melting point of ~ 1148–1153 K [117, 118]. Tin sulfide SnS has two polymorphic modifications. The low-temperature orthorhombic (sp. gr. *Pnma* (D_{2h}^{16})) modification α-SnS is stable at temperatures below ~ 875–878 K. Initially, with a different choice of axial directions, the space group of the α-SnS modification (herzenbergite) was determined as *Pbnm* [117–119]. The unit cell parameters of the low-temperature orthorhombic (sp. gr. *Pnma*) phase of α-SnS are $a = 1.1195–1.1200$ nm, $b = 0.3987–0.3988$ nm, and $c = 0.4332–0.4334$ nm [120, 121]. At a temperature above ~ 878 K, the low-temperature orthorhombic tin sulfide transforms into the high-temperature orthorhombic (sp. gr. *Cmcm*) modification of β-SnS. According to neutron diffraction data [122], the unit cell parameters of high-temperature orthorhombic (sp. gr. *Cmcm*) tin sulfide β-SnS at a temperature of 1000 K are $a = 1.1481$ nm, $b = 0.4173$ nm, and $c = 0.4128$ nm. The unit cell parameters of the α-SnS phase and the coordinates of the Sn and S atoms, transformed from the data for space group *Pbnm* [119] to the data for space group *Pnma*, are given in Table 5. Table 5 also presents the unit cell parameters of the high-temperature β-SnS phase and the coordinates of the Sn and S atoms in it [121].

The authors of Ref. [123] reported the formation of a cubic (sp. gr. $Fm\bar{3}m$) SnS phase with a lattice period of $a = 0.580$ nm in a film epitaxially deposited on an NaCl substrate. The calculation [124] performed within the framework of the density functional theory (DFT) using the generalized gradient approximation (GGA) showed that cubic tin sulfide SnS has a lattice period of $a = 0.575$ nm. In enthalpy of formation (−0.95 eV), cubic SnS sulfide is close to orthorhombic (sp. gr. *Pnma*) α-SnS, which has an enthalpy of formation of −1.03 eV. According to experimental results [125, 126] and theoretical ab initio calculations [127], the formation of a metastable, strongly distorted cubic (sp. gr. $P2_13$) phase of π-SnS is possible in thin films, including 32 formula units of SnS and having a unit cell period of $a = 1.1603–1.1506$ nm. According to Ref. [128], the formation enthalpy of the π-SnS phase is 0.01 eV atom^{-1} higher than that of orthorhombic α-SnS tin sulfide. According to Ref. [128], the thermodynamic stabilization of the π-SnS phase is facilitated by the presence of vacancies in the metallic sublattice.

The unit cells of the orthorhombic phases of α-SnS and β-SnS tin sulfide are shown in Fig. 9.

Lead sulfide is the only compound that exists in the Pb–S system (Fig. 10). It contains ~ 50 at.% of S, has a melting point of 1391 K, and has a narrow homogeneity region [129]. A detailed analysis of the phase diagram of the Pb–S system near 50 at.% of S (see the inset in Fig. 10) shows that the maximum melting point of lead sulfide corresponds to the

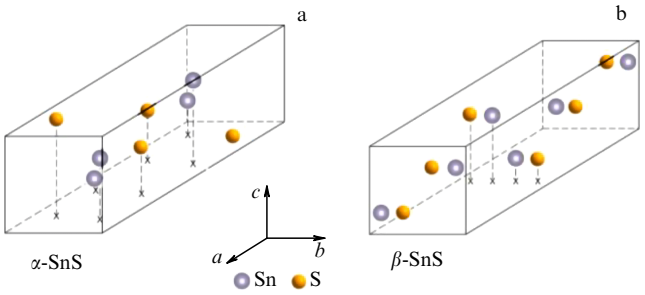

Figure 9. Unit cells of orthorhombic phases (a) α-SnS (sp. gr. *Pnma*) and (b) β-SnS (sp. gr. *Cmcm*) of tin sulfide, constructed by the author of the review based on data from Refs [119, 121].

nonstoichiometric composition $PbS_{0.9998}$. From the data of Ref. [129], it follows that, at a temperature of 1300 K, lead sulfide has a very narrow homogeneity region from 49.9905 to 50.003 at.% of S. Coarse-crystalline (bulk) lead sulfide is considered to be a stoichiometric compound with a negligibly narrow homogeneity region of $PbS_{0.9995–1.0005}$ at 298 K.

Under normal conditions, coarse-crystalline lead sulfide PbS has a cubic (sp. gr. $Fm\bar{3}m$) structure of type *B*1 with a lattice period of $a = 0.59362$ nm [130] (Fig.11a).

Under a pressure of 2.5 GPa, lead sulfide with the *B*1 structure acquires the orthorhombic *B*16 (*B*33) structure, i.e., a phase transition from the cubic (sp. gr. $Fm\bar{3}m$) structure of the *B*1 type to the orthorhombic (sp. gr. *Pnma*) structure of the GeS type is observed [129]. With a decrease in the particle size, the surface energy of the substance increases; therefore, the pressure required to change the crystal structure must increase. Indeed, in PbS nanopowder, the phase transition from the cubic *B*1 structure to the orthorhombic structure begins at a higher pressure of 3.0 GPa [131]. Both phases with the *B*1 and *B*16 (*B*33) structures can exist simultaneously up to 8 GPa. With an increase in pressure to 25 GPa, a second phase transition of lead sulfide to the cubic structure of the CsC1 (*B*2) type is observed [132].

Studies of nanopowders, isolated nanoparticles, and quantum dots of lead sulfide using X-ray and electron diffraction methods [133–137] in combination with high-resolution transmission electron microscopy (HRTEM) data confirm their type *B*1 cubic structure.

The crystal structure of PbS nanofilms was also considered to be a *B*1 type structure for a long time, but studies in recent years have shown that this opinion is erroneous. The crystal structure of ~ 100-nm-thick PbS nanostructured films was quantitatively determined in [138] using different models of the cubic structure. As a result of the quantitative analysis, it was established that the real structure of the PbS nanofilm belongs to the $Fm\bar{3}m$ space group, but the sulfur atoms S in it

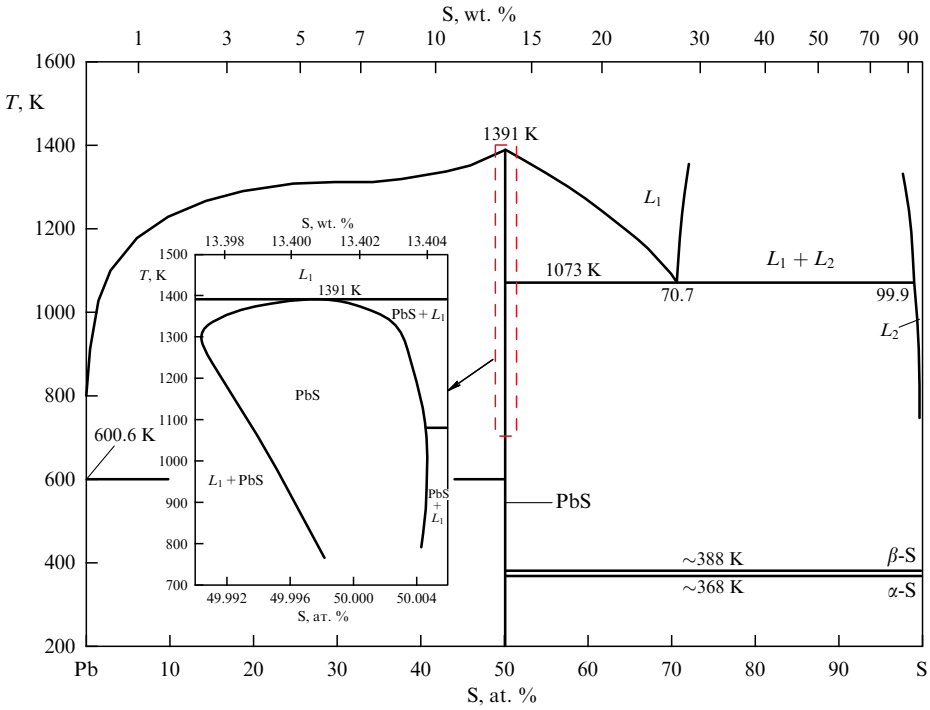

Figure 10. Phase diagram of Pb – S system. Inset shows an enlarged section of diagram near 50 at.% of S, showing presence of a very narrow homogeneity region in lead sulfide. (Figure constructed by the author of the review based on data from Refs [13, 129]).

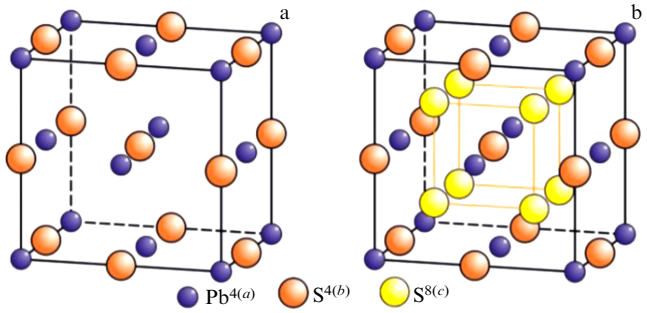

Figure 11. Crystal structures of lead sulfide PbS: (a) unit cell of coarse-crystalline (bulk) cubic (sp. gr. $Fm\bar{3}m$) lead sulfide with structure of $B1$ type (b) distribution of Pb and S atoms in unit cell of cubic (sp. gr. $Fm\bar{3}m$) structure of $D0_3$ type of $PbS \equiv PbS_y^{4(b)}S_{1-y}^{8(c)}$ nanofilm. In unit cell with $D0_3$ type structure, S atoms statistically occupy octahedral positions $4(b)$ with probability y and statistically occupy tetrahedral positions $8(c)$ with probability $(1-y)/2$. (Figure constructed by the author of the review based on data from Refs [13, 138].)

are located not only in octahedral interstices ($4(b)$ positions), but also in tetrahedral interstices ($8(c)$ positions) (Fig. 11b). In such a structure, the probabilities of filling the $4(b)$ and $8(c)$ positions with S atoms are equal to y and $(1-y)/2$, respectively.

Minimization of experimental X-ray diffraction patterns of PbS nanofilms recorded in situ at temperatures from 293 to 423 K with a step of 30–40 K showed that at all temperatures the degrees of filling of positions $4(b)$ and $8(c)$ by S atoms are equal to ~ 0.84 and ~ 0.08, respectively (Table 6).

The value of the convergence factor R_I for all X-ray diffraction patterns did not exceed 0.017. Thus, in the lattice of the PbS film, a hidden nonstoichiometric distribution of S atoms over positions $4(b)$ and $8(c)$ is realized. The new cubic

Table 6. Cubic (sp. gr. $Fm\bar{3}m$) structure of type $D0_3$ of nanostructured PbS film at temperature of 293 K: $a = 0.59395$ nm [138].

Atom	Position and multiplicity	Atomic coordinates			Filling degree
		x/a	y/a	z/a	
Pb	$4(a)$	0	0	0	1
S	$4(b)$	0.5	0.5	0.5	0.84
S	$8(c)$	0.25	0.25	0.25	0.08

(sp. gr. $Fm\bar{3}m$) structure found in lead sulfide nanofilms belongs to the structural type $D0_3$ with a partially disordered (statistical) distribution of S atoms over positions of two types (Fig. 11b). Taking into account the crystal structure of the nanofilm and the degrees of filling the positions $4(b)$ and $8(c)$, the formula of the lead sulfide nanofilm can be represented as $PbS_{0.84}^{4(b)}S_{0.16}^{8(c)} \equiv Pb(S_{0.84}\square_{0.16})^{4(b)}(S_{0.16}\square_{0.84})^{8(c)}$, where $\square$ is a structural vacancy.

Let us consider a model of the $D0_3$ structure of a PbS nanofilm, which includes three unit cells (Fig. 12). This model cell contains 12 octahedral interstices, i.e., 12 positions (b). In a cubic structure with the space group $Fm\bar{3}m$, the number of tetrahedral interstices is twice the number of octahedral interstices. Therefore, for 12 octahedral interstices, there are 24 tetrahedral interstices, i.e., 24 positions (c). The filling of positions (b) and (c) by S atoms with probabilities of ~ 0.84 and ~ 0.08 means that, approximately, out of every 12 octahedral interstices, 10 are occupied by S atoms, and two are empty. Two tetrahedral interstices are also occupied by S atoms, and the rest are vacant. The absence of superstructural reflections means that the arrangement of S atoms at positions of each type is disordered, statistical.

Thus, the considered semiconductor sulfides have a non-molecular coordination structure, and some semiconductor sulfides (in particular, copper and silver sulfides) have a

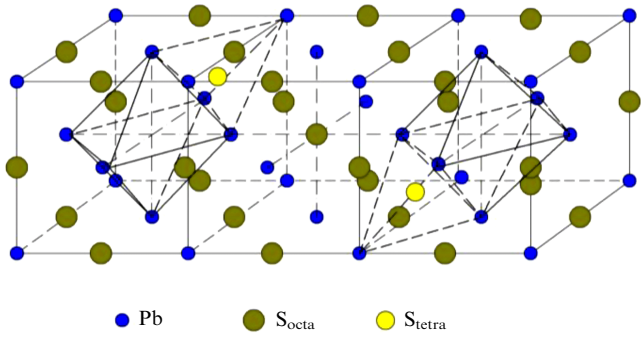

Figure 12. Model of cubic (sp. gr. $Fm\bar{3}m$) structure of type $D0_3$ of the PbS nanofilm: S atoms statistically occupy ten of the 12 octahedral interstices (positions (*b*)) and two tetrahedral interstices (positions (*c*)) out of 24 tetrahedral interstices. The 10 occupied and two empty octahedral interstices, as well as the two occupied tetrahedral interstices, are shown.

nonstoichiometry of the metallic sublattice both in the coarse-crystalline and nanocrystalline states. A nonstoichiometric distribution of sulfur atoms S over two different positions of the nonmetallic sublattice was found in lead sulfide nanofilms. However, due to the lack of study, information on the nonstoichiometry of most nanocrystalline sulfides is still absent. In review [139], using carbides as an example, it was shown that a decrease in the particle size of solid-phase substances, including sulfides, to the nanometer scale leads to the appearance or increase of nonstoichiometry. Among the publications of recent years on the nonstoichiometry of semiconductor sulfides, papers [140–143] are also worth mentioning.

3. Characteristics of electronic structure of semiconductor sulfides

To understand the properties of nanocrystalline semiconductor sulfides, it is useful to know the characteristics of the electronic structure of the corresponding coarse-crystalline semiconductors. An important property of semiconductors is the band gap width E_g. Information on the value of E_g of coarse-crystalline elementary and binary semiconductors obtained before 1971 is summarized in Ref. [144]. In subsequent years, measurements and estimates of the band gap width were carried out mainly in nanostructured semiconductor compounds.

It is known that decreasing the particle size to the nanometer scale noticeably affects the properties of substances [145–147]. From a scientific point of view, not all substances with a particle size in the nanometer range from 1 to 100 nm are nanomaterials, but only those in which size effects are manifested and whose properties differ significantly from the properties of coarse-crystalline substances. In general, size effects unite a complex of phenomena associated with a change in the properties of a substance due to (1) a direct change in the size and morphology of particles, (2) a high development and area of intergranular boundaries, which, with a grain size from 100 to 10 nm, contain from 10 to 50% of the nanocrystalline solid atoms and contribute to the properties of the system, (3) commensurability of the particle size with physical parameters having the dimension of length [145–147]. If the sizes of particles (grains, crystallites) of a solid in one, two, or three directions are commensurate with some characteristic physical parameters that have the dimension of length (size of magnetic domains, electron mean free path, de Broglie wavelength, exciton diameter), then size effects will be observed in the corresponding properties. In semiconductor compounds, the ratio of particle sizes to the exciton size determines whether size effects will be observed in their properties. In other words, when the size of crystalline particles decreases to sizes comparable to the exciton size, the semiconductor crystalline substance passes into a nanocrystalline state.

For example, the size of an exciton in semiconductors is up to tens of nanometers and exceeds the size of a unit cell. This opens the possibility of creating semiconductor sulfide nanomaterials whose properties are changed by regulating the sizes of their constituent structural elements (particles, grains, crystallites).

An exciton is a quasiparticle which is an electronic excitation migrating through a crystal without transferring electric charge or mass. An exciton in a semiconductor is a bound state of an electron and a hole occupying different sites of the crystal lattice. The exciton can be considered an independent elementary particle in cases where the interaction energy of an electron and a hole is of the same order as the energy of their motion, and the interaction energy between two excitons is small compared to the energy of each of them. An exciton in a semiconductor, called a Wannier–Mott exciton, is a bound state of a conduction electron and a hole located at a distance greater than the interatomic distance. Excitons in semiconductors with high permittivity are characterized by a large size (many times greater than the distance between atoms) and low energy.

The characteristic size of a Wannier–Mott exciton (or the Bohr radius of an exciton) in a macroscopic semiconductor crystal is equal to $R_{ex} \approx n^2\hbar^2\varepsilon/\mu_{ex}e^2 = (n^2\varepsilon m_0/\mu_{ex})a_B$, where ε is the permittivity; $\mu_{ex} = m_e m_h/(m_e + m_h)$ is the reduced mass of an exciton; m_e and m_h are the effective masses of an electron and a hole, expressed through the rest mass of a free electron $m_0 = 9.109 \times 10^{-31}$ kg; $a_B = \hbar^2/m_0e^2 = 0.0529$ nm is the Bohr radius;

$$\hbar = \frac{h}{2\pi} = 1.055 \times 10^{-34}\ \text{J s} = 1.055 \times 10^{-27}\ \text{g cm}^2\ \text{s}^{-1} = 6.583 \times 10^{-16}\ \text{eV s}$$

is the Planck constant; and $e = 4.8032 \times 10^{-10}\ \text{cm}^{3/2}\ \text{g}^{1/2}\ \text{s}^{-1}$ is the elementary charge.

If the particle size of the nanostructured sulfide is smaller than the exciton size, then size effects will be observed in the electronic properties of the sulfide, including the band gap width E_g. The quantum size effect in semiconductors, namely the short-wave shift of the exciton absorption lines of CuCl nanoparticles in a glass matrix, was first discovered in Ref. [148].

Biexciton effects also play a significant role in semiconductors. A biexciton is a bound complex of two electrons and two holes. In direct band semiconductors, the formation and decay of biexcitons occur under nonequilibrium conditions.

In an experimental study of the induced conversion of excitons to biexcitons, the sample is excited by laser radiation in the region of interband transitions, where broad one-photon absorption bands are observed, indicating the formation of biexcitons [149]. Resonant excitation of biexcitons in the process of giant two-photon absorption was experimentally detected in the transmission spectra of CdS under laser excitation [150]: against the background of a flat tail of the exciton absorption band, a narrow absorption line

at 2.5499 eV was clearly observed, associated with resonant two-photon absorption and with the creation of a biexciton in cadmium sulfide. For coarse-crystalline (bulk) CdS at a temperature of 2 K, the biexciton binding energy and its excitation energy are 4.4 ± 0.2 meV and 5.0998 eV. With increasing temperature, the biexciton absorption lines disappear from the transmission spectra at 20–25 K due to thermal dissociation of biexcitons and their scattering by phonons. An important tool for studying the structure and spectrum of biexcitons in direct band semiconductors is hyper-Raman (or two-photon Raman) scattering. In Ref. [151], using the example of CdS quantum dots in a glass matrix, it was shown experimentally and theoretically that the biexciton binding energy in semiconductors increases with decreasing quantum dot size. M.G. Bawendi et al. [152] noted that, in nanocrystals, due to the almost exact balance between absorption and emission, the optical gain condition can be achieved only by exciting biexcitons. Note that M.G. Bawendi et al. [153] previously created a method for synthesizing colloidal solutions of nearly monodisperse chalcogenide quantum dots in organic solvents. Among many other papers by M.G. Bawendi, it is necessary to mention studies on the synthesis of core/shell heterostructures based on cadmium telluride and cadmium selenide, cadmium and zinc sulfides, etc. [154–157].

Exciton and biexciton effects in quantum dots of semiconductor chalcogenides have been considered in many studies, including [158–162].

A decrease in the particle size of nanostructured compounds compared to crystallite ones also leads to a transformation of the density of states, which is most clearly manifested in quantum dots. According to Ref. [1], in the regime of strong quantum localization in nanostructured semiconductors, such fundamental properties as the density of electron states and the width of the band gap E_g change. In Refs [163, 164], it was noted that a decrease in the dimensionality of a semiconductor can increase the electron density of states near the Fermi level. Such features in the density of electron states of nanostructured semiconductors can arise because of two- or three-dimensional quantum confinement.

Information on the effective masses of electrons and holes in Cu_2S sulfide is limited to theoretical paper [67], in which the values of m_e and m_h are given for the model cubic chalcocite γ-Cu_2S ($Cu_{32}S_{16}$). The permittivity $\varepsilon = 4.79$ was estimated in Ref. [165] for a thin film of orthorhombic chalcocite Cu_2S. According to the data in Ref. [166], the permittivity ε of the $Cu_{2-x}S$ phase at small values of x is 10–15. Taking into account the data from [67, 165], the reduced mass of the exciton in Cu_2S is equal to $(0.21-0.25)m_0$. The radius of the first exciton state ($n = 1$) is $R_{ex} \approx 1.0-1.2$ nm with $\varepsilon \approx 4.8$ [165] or $R_{ex} \approx 2.5-3.8$ nm with ε from 10 to 15 [166].

The band gap width for indirect and direct transitions in the coronal crystalline sulfide Cu_2S is 1.05–1.30 eV [167–169] and 1.3–1.9 eV [167, 168, 170, 171], respectively.

According to various data [172–174], hexagonal covellite CuS has a band gap width from $\sim 1.2-2.0$ eV for coarse-crystalline samples to 3.0–3.5 eV for nanocrystalline films.

Under normal conditions, coarse-crystalline (bulk) silver sulfide with the acanthite structure α-Ag_2S is a direct semiconductor with a wide band gap E_g and low carrier mobility. For coarse-crystalline acanthite α-Ag_2S, the effective electron and hole masses are $m_e = 0.286m_0$ and $m_h = 1.096m_0$, and the permittivity ε is 5.95 [175]. Taking this into account, the reduced exciton mass μ_{ex} for acanthite α-Ag_2S is $\sim 0.23m_0$. However, the data in [175] on the effective masses of an electron and a hole in α-Ag_2S are most likely not entirely correct, since this paper does not contain any information on estimating the Brillouin zones or measuring the effective masses by the cyclotron resonance method. According to the calculation of the electronic structure of the coarse-crystalline (bulk) monoclinic silver sulfide α-Ag_2S, which was obtained in Ref. [176] within the framework of the density functional theory (DFT) using the generalized gradient approximation (GGA), the effective masses of the electron and hole corresponding to the lower conduction band and the higher valence band (the Γ points of the Brillouin zone) are $m_e = 0.42m_0$ and $m_h = 0.81m_0$, and the band gap width is 0.914 eV. For such values of the effective masses of the carriers, the reduced exciton mass μ_{ex} for acanthite α-Ag_2S is equal to $\sim 0.28m_0$.

The permittivity of silver sulfide is a complex quantity. According to Refs [177, 178], the real part of the permittivity ε in silver sulfide is 8.36 or 8.8, respectively. Considering the value of ε from ~ 6 to ~ 8.8, the characteristic size of the first ($n = 1$) Wannier–Mott exciton R_{ex} in coarse-crystalline acanthite α-Ag_2S is $\sim 1.4-2.1$ nm for $\mu_{ex} = 0.23m_0$ or $\sim 1.1-1.7$ nm for $\mu_{ex} = 0.28m_0$. The exciton diameter is $D_{ex} \approx 2.8$–4.2 nm or 2.2–3.4 nm and is 3–8 times greater than the periods of the unit cell of monoclinic acanthite. According to Ref. [179], the exciton diameter of silver sulfide is ~ 4.4 nm.

The authors of Ref. [176] also found an empirical dependence of the energy of the ground exciton state (deviation of the energy of the ground exciton state from the band gap width of coarse-crystalline Ag_2S), ΔE_{ex}, on the diameter D of the quantum dot of silver sulfide: ΔE_{ex} [eV] $= 4.8366D^{-2.1525} - 0.0959$. The diameter D of the quantum dot in this dependence is taken in nanometers. It follows from this dependence that, in the limit $D \to \infty$, i.e., for coarse-crystalline (bulk) silver sulfide, the exciton binding energy is 0.096 eV.

The band gap width of α-Ag_2S depends on temperature. According to Refs [77, 78], the value of E_g in acanthite α-Ag_2S at a temperature of 300 K is $\sim 0.8-1.0$ eV. The generally accepted band gap width E_g for acanthite α-Ag_2S at 300 K is 0.9–1.1 eV [11].

Under normal conditions, coarse-crystalline (bulk) zinc sulfide is a direct band semiconductor. For coarse-crystalline hexagonal zinc sulfide at $T = 300$ K, the effective masses of the electron and hole are $m_e = 0.28m_0$ and $m_h = 0.49m_0$ [180]. With these values taken into account, the reduced exciton mass μ_{ex} of hexagonal zinc sulfide ZnS is $\sim 0.18m_0$.

The permittivity of hexagonal zinc sulfide at 300 K is $\varepsilon_{11} = \varepsilon_{33} = 8.7$ [181], $\varepsilon_{11} = 8.1$, and $\varepsilon_{33} = 8.5$ [182], or $\varepsilon_{11} = 8.31$ and $\varepsilon_{33} = 8.76$ [183]. According to [180], the permittivity of cubic and hexagonal zinc sulfide is 8.9 and 8.75, respectively. With the reduced exciton mass $\mu_{ex} = 0.18m_0$ and the permittivity ε_{ZnS} from 8.1 to 8.76, in coarse-crystalline zinc sulfide ZnS, the size R_{ex} of the first exciton state is from ~ 2.4 to ~ 2.6 nm; the diameter D_{ex} is $\approx 4.8-5.2$ nm.

The band gap width E_g of cubic α-ZnS at a temperature of 300 K is 3.54–3.76 eV [180, 184]; E_g of hexagonal wurtzite β-ZnS is ~ 3.74–3.91 eV [184, 185].

Coarse-crystalline (bulk) cadmium sulfide is a direct band semiconductor. For coarse-crystalline cadmium sulfide at $T = 300$ K, the electron and hole effective masses are

$m_e = 0.19m_0$ and $m_h = 0.80m_0$ [186], $m_e = 0.21m_0$ [187] or $m_e = 0.205m_0$ and $m_h = 0.81m_0$ [188]. With these values taken into account, the reduced exciton mass μ_{ex} of cadmium sulfide CdS is $\sim 0.16m_0$.

The dielectric constants ε_{11} and ε_{33} of cadmium sulfide, measured by the ultrasonic resonance method at 300 K, are 8.67 and 10.2, respectively [189]. According to ellipsometry measurements [190], $\varepsilon_\perp = 8.28$ and $\varepsilon_\parallel = 8.73$ at 300 K. Considering the generalized data [189–191], the dielectric constant ε of cadmium sulfide at 300 K is ~ 9.0. With the reduced mass $\mu_{ex} = 0.16m_0$ and the dielectric constant $\varepsilon_{CdS} = 9.0$ in coarse-crystalline cadmium sulfide CdS, the size R_{ex} of the first exciton state with $n = 1$ is ~ 3.0 nm; the diameter D_{ex} is ≈ 6.0 nm.

The band gap width of CdS is highly dependent on temperature. A detailed analysis of the temperature dependence $E_g(T)$ for cadmium sulfide was performed in Ref. [192]. According to [192], $E_g(T)$ decreases monotonically from ~ 2.58 to ~ 2.49 eV with a temperature increase from 0 to 300 K. The generally accepted band gap width of CdS at 300 K is ~ 2.42 eV [13].

The trigonal α-HgS and cubic β-HgS phases of mercury sulfide are direct band semiconductors. The coarse-crystalline (bulk) trigonal phase of α-HgS is a wide-band semiconductor with a band gap width of $E_g = 2.0-2.3$ eV [144, 193, 194]. There is no data in the literature on the effective masses of electrons and holes in trigonal α-HgS.

According to Ref. [195], the effective masses of the electron and hole in cubic mercury sulfide β-HgS are $m_e = 0.032m_0$ and $m_h = 0.041m_0$, and the permittivity is $\varepsilon = 11.36$. According to the calculations in [196], the value of ε is 12.9. For the indicated values of m_e, m_h, and ε, the mass and radius of the exciton in cubic β-HgS are $\sim 0.018m_0$ and $\sim 33.4-37.9$ nm. The size (diameter) of the exciton is more than 100 times greater than that of the unit cell of β-HgS sulfide.

According to various data, the band gap of β-HgS is from 0.54 eV [197] to 0.05 eV [198] or −0.15 eV [199] and −0.19 eV [200]. According to calculations [196] using the generalized gradient approximation in the Engel–Vosko scheme, the value of E_g for cubic mercury sulfide β-HgS is −0.1 eV. The small value and even the negative sign of the energy gap in β-HgS is associated with the small spin-orbit splitting in sulfur [198].

Until about the 1970s, orthorhombic tin sulfide α-SnS was identified as an indirect transition semiconductor based on optical measurements. However, later in Ref. [201], a direct transition was discovered in tin sulfide along with an indirect transition.

At $T = 300$ K, the effective masses of a hole in single-crystal α-SnS, depending on the direction, are $m_{ha} = m_{hb} = 0.2m_0$ and $m_{hc} = m_0$ [202–204], and the average effective mass of a hole is $\sim 0.34m_0$. According to Ref. [205], the effective masses of an electron in bulk tin sulfide, depending on the direction, are $m_{ea} = 0.45m_0$, $m_{eb} = 0.16m_0$, and $m_{ec} = 0.20m_0$, and the average effective mass of an electron is $\sim 0.24m_0$. For the above values, the average reduced mass μ_{ex} of an exciton in orthorhombic α-SnS is $\sim 0.14m_0$.

The experimental average value of the permittivity ε at 300 K is 12.5 [206]. According to calculations [205], in coarse-crystalline orthorhombic tin sulfide, it is 11.7, 13.8, and 11.4 for the *a*-, *b*-, and *c*-axes, the average value being 12.3. According to Ref. [204], the permittivity of α-SnS sulfide is 19.5. With the reduced exciton mass $\mu_{ex} = 0.14m_0$ and the permittivity ε_{SnS} from 12.3 to 19.5, in coarse-crystalline tin sulfide, the exciton radius R_{ex} is from ~ 4.6 to ~ 7.4 nm; the diameter D_{ex} is $\approx 9.2-14.8$ nm.

The band gap width E_g of α-SnS sulfide is 2.21 eV [207] or 2.07 eV [208] for the indirect transition. According to calculations [205], the band gap width E_g for the direct transition is 1.32–1.62 eV. In orthorhombic α-SnS films, the band gap widths for the indirect and direct transitions depend on the stoichiometry of the sulfide and vary from 1.07 to 1.25 eV and from 1.30 to 1.39 eV, respectively [204]. According to Ref. [209], the temperature dependence of the indirect optical gap width is described by the function $E_g = 1.21–0.00048T$ [eV].

Under normal conditions, coarse-crystalline (bulk) lead sulfide PbS is a narrow direct band semiconductor. At $T = 4$ K, the effective masses of an electron and a hole in PbS are $m_e = (0.092 \pm 0.012)m_0$ and $m_h = (0.090 \pm 0.015)m_0$ [210]. According to [211], the effective masses of an electron and a hole in bulk lead sulfide at 300 K are $m_e = m_h = 0.105m_0$, so that the exciton mass is $\mu_{ex} = 0.0525m_0$. The permittivity ε of lead sulfide at 300 K is 18 [212], 17.2 [213], 17.0 [211], or 16.4 [214]. At $\mu_{ex} = 0.0525m_0$ and a permittivity ε of $\approx 17-18$ for lead sulfide, the size R_{ex} of the first exciton state with $n = 1$ is $\sim 19\varepsilon a_B$ or 17–18 nm.

According to the results of early studies in the 1950s and 1960s and many other studies summarized by the authors of Refs [212, 215, 216], at a temperature of 300 K in single-crystal PbS and in polycrystalline PbS films, the band gap width E_g for direct transitions is equal to 0.41 and 0.42 eV, respectively.

Generalized parameters of coarse-crystalline sulfides necessary for estimating the exciton size, as well as the exciton sizes in the considered sulfides, are given in Table 7.

The exciton size is proportional to the dielectric constant ε, which increases noticeably in the series $Cu_2S \rightarrow Ag_2S$, $ZnS \rightarrow CdS \rightarrow HgS$, and $SnS \rightarrow PbS$, as well as when transitioning from sulfides of metals of the IB group (Cu, Ag) to sulfides of metals of the IIB group (Zn, Cd, Hg) and to sulfides of metals of the IVA group (Sn, Pb). The exciton masses of the considered sulfides change much less strongly; therefore, the exciton size, like the value of ε, also increases in the series $Cu_2S \rightarrow Ag_2S$, $ZnS \rightarrow CdS \rightarrow HgS$, $SnS \rightarrow PbS$, as well as in the transition from sulfides of copper group metals to sulfides of zinc group metals and further to sulfides of tin group metals. Considering the sizes of excitons, the effects on the electronic properties of the considered sulfides can be observed in fairly large ($\leqslant 15$ nm) nanoparticles of lead sulfide and significantly smaller nanoparticles ($\leqslant 3-4$ nm and $\leqslant 1.5-2$ nm) of zinc and cadmium or copper and silver sulfides, respectively, which is in good agreement with numerous experimental data, summarized in Refs [9, 11–13]. The size effects in the electronic and optical properties are most clearly observed in colloidal solutions of sulfide quantum dots [11, 22–24, 179, 217, 218], in quantum dots dispersed in glass [219, 220] or polymer matrices [221–225], and in sulfide nanofilms [138]. The size effects in various properties of the considered semiconductor sulfides, associated both with the size of excitons and with other factors (enhancement of quantum localization, biexciton effects, transformation of the density of states, influence of the morphology of nanoparticles, change in the type and boundaries of the phonon spectrum) and synthesis conditions, are discussed in Section 4.

Table 7. Characteristics of electronic structure of coarse-crystalline (bulk) semiconductor sulfides at 300 K and exciton radii.

Sulfide	Effective masses of electron and hole		Exciton mass μ_{ex}/m_0	Dielectric constant ε	Band gap width E_g, eV	Literature	Exciton radius R_{ex}, nm
	m_e/m_0 *	m_h/m_0					
Cu_2S	0.30 – 0.37	0.8	0.21–0.25	4.79	1.05–1.30 **, 1.3–1.9 ***	[67, 165, 167 – 171]	~ 1.0 – 1.2
α-Ag_2S	0.286	1.096	0.227	~ 6.0 – 8.8	0.9 – 1.1	[11, 77, 78, 175, 177, 178]	1.4–2.1
α-Ag_2S	0.42	0.81	0.277	~ 6.0 – 8.8	0.914	[176 – 178]	1.1–1.7
β-ZnS	0.28	0.49	0.18	8.10–8.76	3.74–3.91	[7, 180 – 185]	2.4–2.6
α-ZnS	-"-	-"-	-"-	8.9	3.54–3.76	[7, 180, 184]	2.6
β-CdS	0.19–0.21	0.80–0.81	0.16	9.0	2.42–2.49	[13, 186 – 192]	3.0
β-HgS	0.032	0.041	0.018	11.36–12.90	from −0.2 to 0.5	[193–200]	33.4–37.9
α-SnS	0.24	0.34	0.14	12.3, 19.5	2.1–2.2 **, 1.3–1.6 ***	[201–208]	~ 4.6 – 7.4
PbS	0.105	0.105	0.0525	16.4 – 18.0	0.41–0.42	[210–216]	17–18

* $m_0 = 9.1 \times 10^{-31}$ kg (rest mass of a free electron)
** band gap width for indirect transitions
*** band gap width for direct transitions

4. Size effects in properties of nanostructured sulfides

According to Ref. [166], the exciton radius in $Cu_{2-x}S$ is from 3.5 to 5 nm. According to a more accurate estimate, the maximum exciton radius is 3.8 nm (see Table 7), and the exciton diameter in Cu_2S sulfide does not exceed 8 nm, so actual, not imagined, quantum size effects in Cu_2S can be observed for particles 8 nm or less in size. There is no information in the literature on the production and optical properties of nanostructured Cu_2S sulfide ($Cu_{2-x}S$) with nanoparticles of this size. Paper [166] describes the synthesis of CuS, $Cu_{1.97}S$, and $Cu_{1.8}S$ nanocrystals by sonoelectrochemical and hydrothermal methods and by thermolysis. According to Ref. [166], the size of nanocrystals synthesized by the sonoelectrochemical method ranges from ~ 5 to ~ 15 nm, the diameters of nanoparticles obtained by the hydrothermal method are ~ 20 – 25 nm, and the diameters of nanoparticles obtained by thermolysis reach ~ 30 nm. A broad peak at about 400–600 nm was observed in all measured UV-Vis absorption spectra of synthesized copper sulfide nanocrystals, and for smaller nanocrystals synthesized by sonoelectrochemical and hydrothermal methods, the position of the peak was somewhat shifted to the short-wave region, which, according to the authors of Ref. [166], can be considered a blue shift. However, there is no quantitative processing of the UV-Vis absorption spectra and no estimate of the band gap width in Ref. [166]. In Ref. [49], a significant blue shift was detected in the UV-Vis absorption spectra of hexagonal covellite CuS nanoparticles ~ 17 – 19 nm in size; the calculated band gap energies were ~ 4.3 eV. Since the size of CuS nanoparticles is quite large (much larger than the exciton diameter), this result raises serious doubts. In general, there is no reliable information on quantum size effects in the literature on nanocrystalline copper sulfide.

Much more reliable are the results concerning the dependence of the band gap of $Cu_{2-x}S$ sulfides on their composition. An increase in the band gap occurs with an increase in the value of x in coarse-crystalline (bulk) copper sulfides: E_g is equal to 1.2 eV for Cu_2S, 1.5 eV for $Cu_{1.8}S$, and 2.0 eV for CuS [166]. The optical properties of CuS calculated in [226] are in reasonable agreement with the experimental results [166].

The optical absorption spectra of copper sulfide nanoparticles $Cu_{2-x}S$ of the same size (13.0–13.7 nm) but different composition (Fig. 13) were obtained in Ref. [227]. For copper sulfide nanoparticles, observed in the absorption spectra is a plasmonic band associated with a change in the density of charge carriers, the holes. From Fig. 13, the shift of the absorption peak from 1090 nm for $Cu_{1.1}S$ to 1250 nm for Cu_2S is clearly visible.

In recent years, CuS nanoparticles with different morphologies have attracted attention due to their potential for use in studying cancer tumors [20]. The potential for biomedical application of nanostructured copper sulfide is related to its photoconversion efficiency, i.e., the ability to

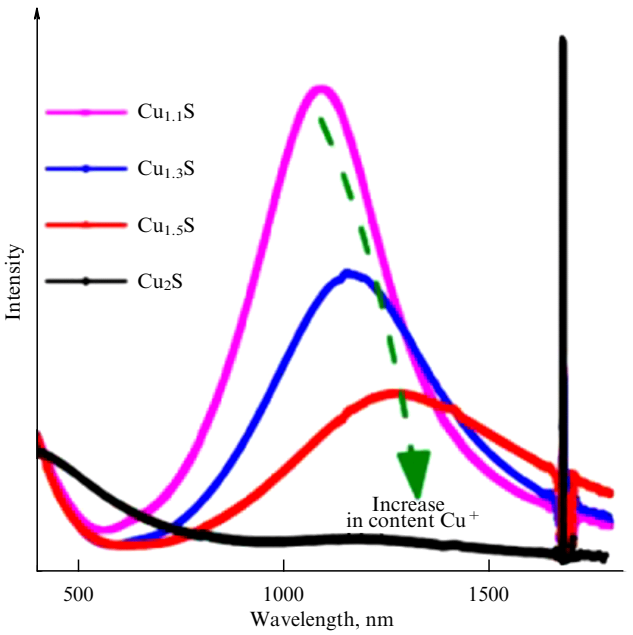

Figure 13. Plasmon band shift as a function of copper sulfide composition. Strong peak at 1700 nm is due to the solvent. (Reproduced from [227] with permission from American Chemical Society.)

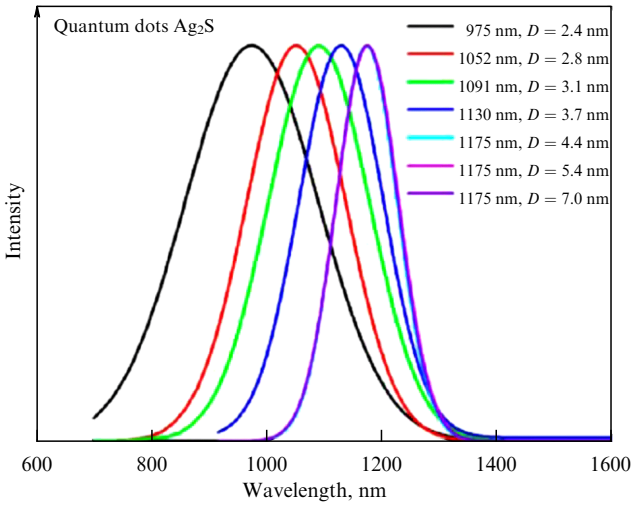

Figure 14. Photoluminescence emission spectra change depending on size of Ag_2S quantum dots excited by 785-nm radiation. Quantum dot sizes and wavelengths corresponding to maxima of photoluminescence peaks are indicated. (Reproduced from [179] with permission from American Chemical Society.)

convert NIR radiation into thermal energy, which can then be used to remove cancer cells [228]. In recent paper [229], CuS nanoparticles with a size of 11 ± 3 nm were proposed to be used as an effective contrast agent in the study of biological tissues. CuS nanoparticles are promising for water purification by photocatalytic decomposition (photodegradation) of pollutants (rhodamine, methylene, etc.), even in natural sunlight radiation [228, 230].

The exciton diameter in silver sulfide Ag_2S is about 4 nm (see Table 7), so obvious size effects in the electronic properties can be observed for sulfide nanoparticles smaller than 4 nm. As an example, Fig. 14 shows the change in photoluminescence emission spectra depending on the size of the Ag_2S quantum dots [179]. The position of the fluorescence maximum of the Ag_2S quantum dots changes from $\sim$ 975 to $\sim$ 1175 nm with an increase in their size D from 2.4 to 4.4 nm. With a further increase in the size of quantum dots from 4.4 to 7.0 nm, the position of the photoluminescence peaks remains unchanged and corresponds to 1175 nm.

The continuous blue shift of the photoluminescence of the Ag_2S quantum dots from 1175 to 975 nm can be associated with the enhancement of the quantum confinement effect and an increase in the band gap E_g due to a decrease in the size of the Ag_2S quantum dots. The almost constant position of the photoluminescence peaks at 1175 nm for the Ag_2S quantum dots with a boundary size of 4.4 nm or more is evidence of a transition from the strong quantum confinement regime to the weak one. Accordingly, the exciton radius R_{ex} of silver sulfide Ag_2S can be experimentally estimated as half or less than half the boundary size of 4.4 nm, i.e., $\leqslant$ 2.2 nm, which is in good agreement with the estimate of R_{ex} given in Table. 7. A similar dependence of the photoluminescence of Ag_2S quantum dots on their size in the range of 2.3–15.0 nm is given in Ref. [11]. The Ag_2S quantum dots described in Ref. [11] were obtained in colloidal solutions of silver nitrate and sodium sulfide using the technique from [218]. With an increase in the size of Ag_2S quantum dots from 2.3 to 4.2 nm, the photoluminescence peaks shift from$\sim$ 960 to $\sim$ 1170 nm, but, with a further increase in the size of the quantum dots, the position of these peaks remains virtually unchanged and corresponds to 1166–1176 nm. According to Ref. [231], the photoluminescence peak of Ag_2S quantum dots $\sim$ 1.5 nm in size is observed at a wavelength of $\sim$ 640 nm.

The effect of the Ag_2S particle size on the position of the photoluminescence peak [179] agrees with the experimental data [218] on the size dependence of the band gap width of silver sulfide, determined from the optical reflectance spectra of Ag_2S nanopowders with an average particle size of $\sim$ 500, $\sim$ 90, $\sim$ 60, and $\sim$ 17 nm. A quantitative analysis of the experimental data, carried out in the wavelength range from 650–700 to 1400–1500 nm, showed that the gap width E_g for Ag_2S powder with a particle size of $\sim$ 500 nm is $\sim$ 0.88 eV and coincides with the value of $E_g \cong 0.9$ eV for bulk silver sulfide α-Ag_2S. For Ag_2S nanopowders with particle sizes of $\sim$ 90, $\sim$ 60, and $\sim$ 17 nm, the value of E_g was $\sim$ 0.96, $\sim$ 1.21, and $\sim$ 1.67 eV. The presence of a blue shift of the optical absorption band in such rather coarse-particle nanopowders is not entirely clear. The increase in E_g observed in [218] may be due not only to a decrease in the size of the nanoparticles, but also to the peculiarities of the synthesis, which was carried out by precipitation from aqueous solutions of $AgNO_3$ and Na_2S with a slight excess of sodium sulfide in the presence of sodium acetate. It is known in [232, 233] that, with an excess of sulfur, the formation of S–S bonds is possible, and the resulting S_2^{2-} and S_n^{2-} particles will be adsorbed on the Ag_2S surface, then the Ag^+ ions will react with them, and this can lead to the formation of compounds Ag_2S_2 and Ag_2S_n, which increase the band gap width of Ag_2S. The presence of Ag_2S clusters of the $(AgS)_n$ type in nanopowders was indirectly confirmed by Raman spectroscopy data [234].

The generation of biexcitons by high-energy photons and multiphoton absorption in Ag_2S quantum dots was studied in Ref. [235]. Regardless of the size of the Ag_2S quantum dots, two different lifetimes of $\sim$ 10 and 135–175 ps were obtained, indicating the existence of weakly bound and strongly bound excitons.

In addition to size effects in the electronic and optical properties, size effects in such lattice properties as the coefficient of thermal expansion and heat capacity were found in nanostructured silver sulfide. The influence of small particle size on these properties of Ag_2S is associated with changes in the type and boundaries of the phonon spectrum. Low-frequency modes that are absent in the spectrum of a bulk crystal appear in the phonon spectrum of small particles [145, 146]. According to Refs [145, 146, 236], waves with a length not exceeding twice the largest particle size D can arise in nanoparticles, i.e., $\lambda \leqslant 2D$; therefore, on the side of low-frequency oscillations, the phonon spectrum is limited by a certain minimum frequency $\omega_{min} \geqslant 2\pi c_t/(2D)$, where c_t is the propagation velocity of transverse elastic oscillations (the transverse speed of sound). There is no such limitation in bulk crystals. In addition, the phonon spectrum is limited at high frequencies.

In Ref. [237], considering the above limitations of the phonon spectrum, it was shown that the heat capacity and thermal expansion coefficient of a nanocrystalline substance are functions not only of the temperature T, but also of the small particle size D.

The authors of [92, 238] experimentally established that the average thermal expansion coefficient α_{aver} and heat capacity C_p of nanocrystalline silver sulfide in the studied temperature range of 293–970 K are greater than those of coarse-crystalline silver sulfide (Fig. 15). A similar effect, namely, a thermal expansion coefficient α of a PbS nanofilm

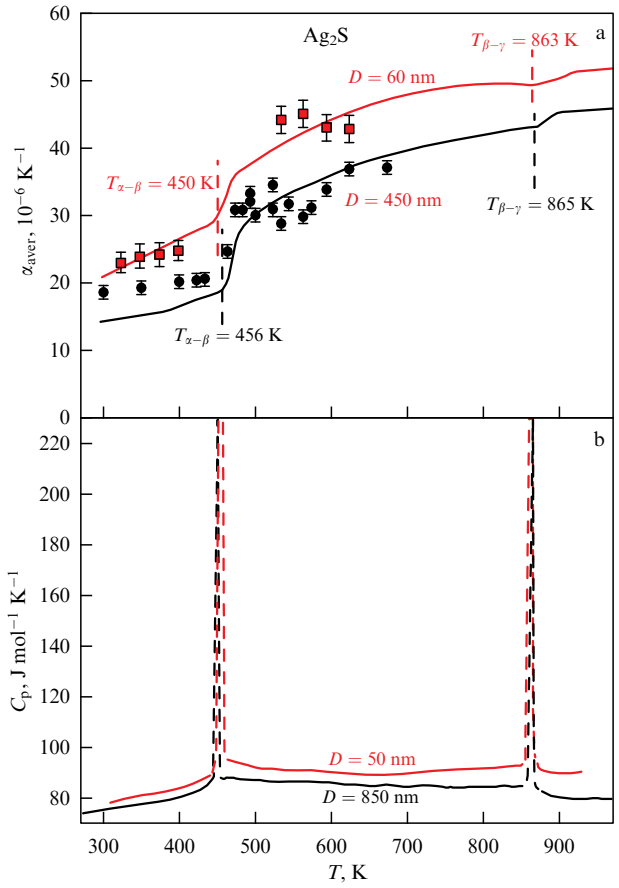

Figure 15. Changes in (a) average thermal expansion coefficient α_{aver} and (b) molar heat capacity C_p of nanocrystalline and coarse-crystalline silver sulfide in temperature range of 293–970 K. For comparison, expansion coefficients α_{aver} of coarse-crystalline (circles) and nanocrystalline (squares) silver sulfides measured by high-temperature X-ray diffraction are shown. Temperatures $T_{\alpha-\beta}$ and $T_{\beta-\gamma}$ of phase transitions α-Ag_2S–β-Ag_2S and β-Ag_2S–γ-Ag_2S are shown by vertical dashed lines. (Figure constructed by the author of the review based on data from Refs [92, 238].)

that is ~ 1.7 times greater than that of bulk coarse-crystalline PbS, was observed by the authors of Ref. [237].

A very interesting result is the effect of the small particle size of silver sulfide with an acanthite structure on the appearance of nonstoichiometry in the metallic sublattice of the sulfide, discovered in [239]. A thorough analysis of the crystal structure of silver sulfide nanopowder with an average particle size of 43 ± 6 nm, performed in [239], showed that the degrees of filling of the metallic sublattice positions by silver atoms are slightly less than 1, being $\sim 0.96-0.97$. This means that silver sulfide nanoparticles with a size of less than ~ 50 nm are nonstoichiometric, have a composition of $\sim Ag_{1.93}S$, and contain vacant sites in the metallic sublattice. Measurements of the positron lifetime in nanocrystalline silver sulfide with a particle size of ~ 50 nm [93] confirmed the presence of vacancies in the metallic sublattice of this compound. Symmetry analysis of the crystal structures of acanthite α-Ag_2S and argentite β-Ag_2S, carried out taking into account the nonstoichiometry of the silver sublattice in these phases, showed that the argentite–acanthite transformation can be considered a disorder–order transition in two sublattices of argentite (non-metallic and metallic), complicated by static displacements of sulfur and silver atoms.

The estimated exciton radius in β-ZnS sulfide is ~ 2.5 nm (see Table 7); the same R_{ex} value for zinc sulfide is given in Ref. [240]. Due to the small size of the exciton, size effects on the electronic and optical properties of zinc sulfide can be observed in quantum dots with a diameter of 5 nm or less, which are quite difficult to synthesize. Therefore, most of the studies on nanostructured zinc sulfide are associated with the study of its properties, depending on the morphology, which is very diverse (from nanospheres to nanowires, nanofibers, nanotubes, nanorods, nanobelts, nanoribbons, and films). Indeed, in reviews [4, 5, 7] on nanostructured ZnS, the main focus is on its morphology.

The effect of the size of ZnS nanoparticles (nanocrystallites) on the band gap width was considered in experimental and theoretical papers [241–245]. In Ref. [241], zinc sulfide nanocrystallites with sizes of 1.8 ± 0.1, 2.2 ± 0.1, and 3.0 ± 0.2 nm were synthesized from zinc acetate and thioglycerol dissolved in dimethylformamide using sodium sulfide. Measurements of the UV-vis optical absorption spectra showed that the band gap width E_g of zinc sulfide with nanocrystallites with sizes of 3.0, 2.2, and 1.8 nm increases from 4.3 to 4.55 and 4.85 eV, respectively. Thus, the quantum confinement effect is observed in ZnS nanocrystallites, leading to an increase in the band gap E_g with a decrease in the nanocrystallite size. According to Ref. [242], the value of E_g for a 2-nm zinc sulfide nanocrystallite is 4.5 eV. The experimentally observed blue shift of the absorption band of ZnS nanocrystallites was later confirmed by theoretical calculations [243]. An increase in the band gap width E_g from 3.7 to 3.9 and 4.3 eV with a decrease in the size of ZnS nanoparticles from 7.9 to 5.6 and 5.1 nm was discovered in Ref. [245].

The different changes in E_g, depending on both the size and morphology of zinc sulfide nanotubes, nanowires, and nanosheets, follow from calculations [244]. For example, according to calculations performed in the local density approximation (LDA), the value of E_g in ZnS nanowires with diameters of ~ 0.82, ~ 1.19, ~ 1.99, and ~ 2.66 nm increases relative to the band gap width $E_{g\text{-bulk}}$ of coarse-crystalline (bulk) ZnS by ~ 0.98, ~ 0.78, ~ 0.51, and ~ 0.26 eV, respectively. An increase in the diameter of single-layer ZnS nanotubes from 0.79 to 1.15 and 1.88 nm also leads to an increase in E_g of single-layer ZnS nanotubes relative to $E_{g\text{-bulk}}$ by 0.96, 0.86, and 0.80 eV, i.e., by a slightly larger value.

Biexciton emission was discovered in [246] in the photoluminescent properties of ZnS single crystals irradiated with a laser with a wavelength of 325 nm (excitation energy of 3.814 eV). The emission line detected at an energy of 3.791 eV has a biexciton nature, which is confirmed by the superlinear increase in intensity with increasing excitation power. The binding energy of the biexciton and its lifetime in ZnS at a temperature of 12 K are about 9 meV and 52 ps, respectively [246].

In monograph [247], it is indicated that the exciton radius for cadmium sulfide is in the range of $\sim 2.1-4.5$ nm. According to Ref. [248], for CdS, the exciton radius is 3.0 nm, which agrees with the estimate $R_{ex} = 3$ nm (see Table 7). Considering the value of R_{ex}, size effects in the electronic and optical properties of cadmium sulfide can be detected when studying nanocrystals and quantum dots with a diameter of 6 nm or less.

The quantum size effect in semiconductors, namely the short-wave shift of the exciton absorption lines of CuCl nanoparticles in a glass matrix, was discovered in Ref. [148].

Cadmium sulfide is exactly the semiconductor in which size effects arising in the electronic and optical properties when CdS particles are reduced to the nanoscale have been discovered and explained in detail [186, 187, 249–254]. According to a theoretical model [249] that takes into account the dispersion of nanoparticle sizes, the effective band gap width E_g increases with decreasing nanoparticle radius R: $E_g = E_{g0} + 0.71\pi^2\hbar/(2\mu_{ex}R^2)$, where E_{g0} is the optical band gap width in the coarse-crystalline semiconductor. This leads to a blue shift of the absorption band edge. Later, Bruce [186, 253] proposed a formula for estimating the magnitude of the absorption band edge shift depending on the nanoparticle size: $\Delta E = \pi^2\hbar/(2\mu_{ex}R^2) - 1.78e^2/(\varepsilon R)$.

The density of states transformation and the absorption band blue shift with decreasing CdS nanoparticle size were discovered by L. Bruce [186]. For CdS nanoparticles with sizes from 1.5 to 40 nm, dispersed in a glass matrix, the blue shift increased with decreasing particle size and was 0.8 eV for nanoparticles with a size of 1.5 nm [186]. There were many subsequent publications on size effects in nanostructured CdS; only a few will be mentioned here.

According to Ref. [254], the band gap width E_g corresponding to CdS nanoparticles with sizes of ~ 5, ~ 2, and ~ 0.7 nm is equal to 2.76, 3.57, and 3.85 eV, respectively. A blue shift of the absorption band with decreasing size of CdS nanoparticles was observed in Ref. [255].

In Ref. [256], cadmium sulfide nanocrystals with sizes from 2.0 to 5.3 nm were synthesized from cadmium oxide and sulfur. Measurements of UV-vis optical absorption and photoluminescence spectra revealed a systematic shift of the observed bands to shorter wavelengths with decreasing nanocrystal size. The experimentally observed blue shift of the absorption band and the transformation of the density of states of CAS nanocrystals were confirmed theoretically [243]. A shift of the absorption band to shorter wavelengths (Fig. 16) and, correspondingly, higher energies with decreasing size of CdS quantum dots was discovered in Ref. [257].

Fluorescence of cadmium sulfide quantum dots from 2 to 6 nm in size obtained from colloidal solutions of cadmium chloride $CdCl_2$ and sodium sulfide Na_2S was studied in Refs [258, 259]. The spectra contained a narrow fluorescence peak and a broad long-wavelength peak. The authors of Refs [258, 259] noted the presence of a size effect in the fluorescence spectra. A study of optical absorption and photoluminescence of CdS nanoparticles obtained in a glass matrix [260] revealed a blue shift of the optical absorption band. For CdS nanoparticles 4 and 6 nm in size, the estimated band gap width was ~ 2.8 and ~ 2.6 eV. An increase in the size of CdS nanoparticles was accompanied by a shift of the photoluminescence band to the long-wavelength region, confirming the presence of a size effect.

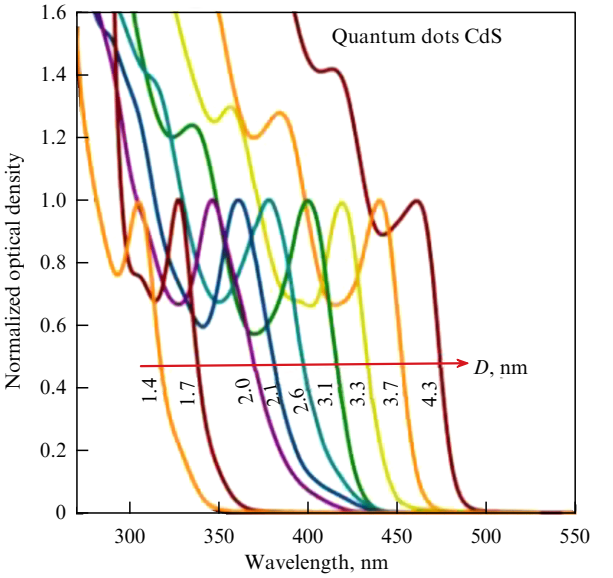

Figure 16. Absorption spectra of CdS quantum dots with sizes from 1.4 to 4.3 nm (direction of increasing quantum dot size is shown by the arrow). (Figure constructed by the author of the review based on data from Ref. [257].)

According to Refs [57–59, 100], the small (less than 10 nm) size of CdS nanoparticles affects their crystal structure by forming a specific disordered hexagonal structure with random (nonperiodic) alternation of close-packed atomic planes. The features of this disordered structure of CdS nanoparticles are described in Section 2.2.

The estimated exciton radius in cubic mercury sulfide β-HgS is 34–38 nm (see Table 7). With such a large value of R_{ex}, size effects in the electronic and optical properties of β-HgS sulfide can be observed for fairly large particles smaller than 70 nm. However, there are few studies on the quantum size effect in mercury sulfide. Apparently, this is due to the toxicity of mercury compounds.

In Ref. [194], nanocrystalline mercury sulfide films with a cubic β-HgS structure and an average crystallite size of 15 nm were synthesized. The band gap width E_g, found from the optical absorption spectra of two different films, was 1.38 and 2.06 eV. According to Ref. [194], the observed noticeable increase in E_g in MO nanofilms compared to $E_{g\text{-bulk}}$ in coarse-crystalline (bulk) β-HgS is due to the quantum size effect.

As is shown in Ref. [194], β-HgS quantum dots with an average size of 4.0 ± 0.5 according to electron microscopy data or 21 ± 3 nm according to X-ray diffraction data have $E_g = 1.21$ eV. Strong absorption in the ultraviolet region at a wavelength of 356 nm, corresponding to $E_g = 3.2$ eV, was found in the UV-vis absorption spectra of β-HgS nanoparticles with an average size of ~ 39 nm [261].

The authors of Ref. [262] synthesized trigonal sulfide α-HgS nanoparticles with a size of $\sim 8-9$ nm. Measurements of the optical absorption spectra revealed a blue shift of the absorption band and an increase in the band gap width by 0.1–0.2 eV relative to E_g of coarse-crystalline (bulk) α-HgS sulfide. Thus, the quantum size effect is also observed for trigonal mercury sulfide α-HgS.

The exciton diameter in tin sulfide α-SnS is $\sim 9-15$ nm (see Table 7); therefore, obvious size effects in the electronic properties can be observed for tin sulfide nanoparticles smaller than 10–15 nm.

In [263], orthorhombic (sp. gr. *Pnma*) tin sulfide α-SnS nanocrystals with a size of 3.2–4.0 nm were precipitated from a solution of $SnCl_2$ in triethanolamine with sodium sulfide Na_2S. Analysis of the UV-Vis optical absorption spectra revealed a strong blue shift, corresponding to the width of the direct band gap of SnS nanocrystals equal to 1.74 eV. Calculation of the optical width of the band gap E_g, depending on the size of the SnS nanocrystals, experimentally confirmed the quantum size effect and an increase in E_g from ~ 1.42 to ~ 2.34 eV with a decrease in the size of the nanoparticles from 10 to 2 nm [263]. According to calculations [205], an increase in the number of SnS layers in model single- and double-layer structures is accompanied by a decrease in the band gap from 2.72 to 1.57 eV, which is a

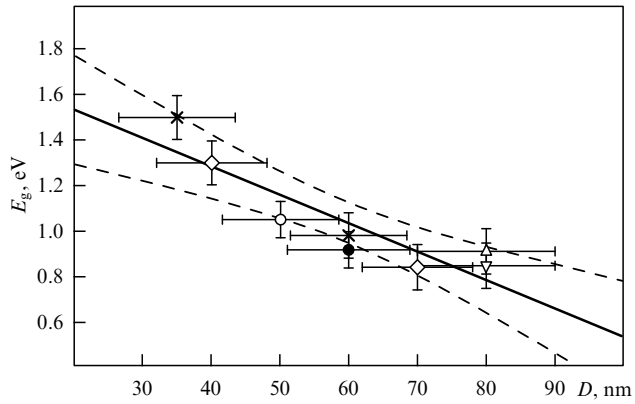

Figure 17. Change in band gap width E_g, in PbS nanofilms with nanoparticles of different sizes D. Dashed curves show 95% confidence interval for determining E_g as a function of particle size D. (Reproduced from [138] with permission from Elsevier.)

manifestation of the size effect. A small increase in E_g, to 1.6–1.7 eV for tin sulfide films with a particle size of ~ 45 nm compared to the band gap width of ~ 1.5 eV for coarse-crystalline (bulk) SnS, discovered in [264, 265], is most likely not due to the size effect, since tin sulfide particles are several times larger than the exciton size. The most likely cause of the observed small increase in E_g [264, 265] may be a change in the phase composition of the films from SnS to Sn_2S_3.

The exciton radius in lead sulfide PbS is $\sim 17-18$ nm (see Table 7), and the exciton diameter does not exceed 36 nm, so quantum size effects can be observed in the electronic and optical properties of nanostructured lead sulfide with particles smaller than ~ 35 nm. The large exciton size and small effective masses of charge carriers (electrons and holes) in PbS nanofilms facilitate charge delocalization and high carrier mobility.

A study of the optical transmission and absorption in PbS nanofilms with different average particle sizes [138] showed that a decrease in the particle size is accompanied by a shift in the absorption band to shorter wavelengths and an increase in E_g, i.e., a blue shift (Fig. 17).

The average size of PbS particles in nanofilms [138] is approximately twice the exciton size, but the band gap width E_g is noticeably larger than in coarse-crystalline (bulk) PbS sulfide. The reason for this is the noticeable dispersion of the nanoparticle size and the presence of small particles smaller than $\sim 10-30$ nm in the nanofilms, which cause an increase in the band gap width. A more pronounced size effect was observed in isolated PbS nanoparticles of 18, 12, and 8 nm in size, dispersed in a polymer matrix [266]. For such nanoparticles, the value of E_g was ~ 2.4, ~ 2.62, and ~ 2.8 eV. According to [267], colloidal PbS nanoparticles with a size from 2.4 to 3.0 nm, synthesized in an aqueous heptane microemulsion, have a band gap width of 3.45–3.30 eV. A strong dependence of the band gap width E_g in colloidal quantum dots of PbS and, especially, of PbSe is noted in the review [23] and Ref. [268].

Exciton effects in PbS quantum dots associated with the generation of multiple excitons are described in [269]. At an irradiating photon energy smaller than the band gap width E_g, a quantum dot can absorb more than one photon with the formation of several excitons. The photon energy is too low to create multiple excitons, but sufficient for the emergence of biexcitons in PbS with a lifetime of ~ 80 ps. The generation of multiple excitons in PbS quantum dots was observed at a photon energy 3.9 times greater than E_g.

The decrease in the size of PbS nanoparticles in the films led to a change in the crystal structure of lead sulfide [138]. The new cubic (sp. gr. $Fm\bar{3}m$) structure found in PbS nanofilms belongs to the $D0_3$ structural type. Taking into account the crystal structure of the nanofilm and the degrees of filling of positions $4(b)$ and $8(c)$, the formula of the lead sulfide nanofilm can be represented as $PbS^{4(b)}_{0.84}S^{8(c)}_{0.16} \equiv Pb(S_{0.84}\square_{0.16})^{4(b)}(S_{0.16}\square_{0.84})^{8(c)}$, where $\square$ is a structural vacancy.

Regulation of the band gap of semiconductor sulfides allows significantly expanding their application, and the main way of such regulation is to reduce the size of sulfide nanoparticles. Another way is to create composite (hybrid) sulfide nanomaterials like mutual solid solutions and heteronanostructures. A large number of heteronanostructures have been created on the basis of zinc sulfide: isolated ZnSe/ZnS nanoparticles with a size of ~ 5 nm [270], Mn-doped ZnS:Mn^{2+} quantum dots [271], CdSe/ZnS microspheres and MnS/ZnS core/shell nanostructures with high photoluminescence [272, 273], green and red light-emitting CdSe/ZnS/CdSZnS and CdSe/CdS/ZnS/CdSZnS heteronanostructures [274], and ZnS/Ag_2S heteronanostructures [275]. Note that CdS is often one of the components of heteronanostructures with zinc sulfide. Cadmium sulfide CdS also forms many heteronanostructures [276–278]. Recently, the production of nanostructured sulfide solid solutions of $Cu_xPb_{1-x}S$ [279], CdPbS [280], CdZnS [281], $Ag_xPb_{1-x}S$ [282], Cu_2SnS_3, Cu_2ZnSnS_4 [283], and many others, as well as nanostructured spherical ZnS particles [284], has been developed.

Recent publications on the synthesis, properties, and applications of quantum dots of CuS and Cu_2S [285, 286], Ag_2S [287, 288], ZnS [289, 290], CdS [291–293], HgS [294, 295], SnS [296, 297], and PbS [298, 299] confirm the relevance of studies of the nanostate of sulfide semiconductors.

5. Conclusions

Sulfide nanostructures retain all the advantages of coarse-crystalline semiconductor sulfides, enhancing their applied properties and expanding the scope of application.

Control of the crystal structure and morphology of sulfides, especially nanostructured ones, plays an important role in achieving the desired electronic and lattice properties, since reducing the particle size to the nanoscale can modify the structure, changing its stoichiometry and even symmetry.

The exciton size is a characteristic parameter of the electronic structure, which allows critical evaluation of the observed changes in the properties of nanocrystalline sulfides and relating them to the size of the nanoparticles. The exciton mass of copper, silver, zinc, cadmium, and tin sulfides is $\sim 0.15-0.25m_0$, whereas in mercury and lead sulfides the exciton mass is noticeably smaller, being $\sim 0.02-0.05m_0$. Due to the small exciton mass and high permittivity, mercury and lead sulfides have the largest excitons, with a diameter of ~ 35 to ~ 75 nm. This allows easy control of the electronic properties of nanostructured mercury and lead sulfides by reducing the size of the nanoparticles to 40–70 nm or less. Various methods for synthesizing HgS and PbS sulfides with nanoparticles of these and smaller sizes are well developed.

The exciton diameter in copper, silver, zinc, cadmium, and tin sulfides is less than 8–10 nm, and size quantum effects in these compounds are experimentally observed for nanoparti-

cles of these and smaller sizes. Due to the difficulty of synthesizing very small nanoparticles, the properties of nanostructured copper, silver, zinc, and tin sulfides are controlled mainly by doping and creating composite nanostructures.

The transition from bulk sulfides to nanocrystalline ones leads to transformation of the density of states, an increase in the band gap width, and a blue shift of the absorption spectral band. Another effect of the transition of sulfides to the nanostate is the appearance or increase in their nonstoichiometry, which affects the phonon spectrum and lattice properties.

The smallest sulfide nanoparticles (colloidal quantum dots) with a size of less than 5 nm are obtained in colloidal solutions. The colloidal method of synthesis in organic solvents led to a revolution in the production of colloidal quantum dots, which was noted by the 2023 Nobel Prize in Chemistry "for the discovery and synthesis of quantum dots." The laureates of the prize were M.S. Bawendi, L.E. Brus, and our compatriot A.I. Ekimov. In 1981, A.I. Ekimov, together with A.A. Onushchenko, became the first to find that CuCl nanoparticles in a glass matrix absorbed light of different wavelengths, depending on their size. Two years later, L.E. Brus and colleagues found that the optical properties of CdS nanoparticles in a colloidal solution differ from those of coarse-crystalline CdS and change as the nanoparticles grow. M.G. Bawendi and co-authors developed a reproducible method for synthesizing colloidal nearly monodisperse quantum dots of cadmium sulfide, selenide, and telluride with a narrow size distribution in organic solvents such as trioctylphosphine and trioctylphosphine oxide.

An important task is to ensure a homogeneous morphology of nanostructured sulfides, which significantly depends on the production method, composition, and crystal structure. Zinc and lead sulfides have a particularly diverse morphology of nanostructures. In general, the morphology of particles is determined by minimizing their surface energy and kinetic growth conditions. Nanoparticles are usually thermodynamically nonequilibrium, so their diverse morphology is a consequence of metastability, i.e., the system is in one local minimum of free energy or another. Varying the kinetic parameters of synthesis (temperature, pressure, reagent concentration, synthesis duration, supersaturation and pH of solutions, and heating and cooling rates) allows controlling the shape of nanoparticles.

Sulfides are widely used in micro- and optoelectronics to produce elements for various optical instruments and devices in biology and medicine. They are used to create infrared sensors and photodetectors, near and medium infrared lasers, nonvolatile memory devices, ultrasound detectors, thermoelectric converters, and optical switches. These sulfides are used as phosphors for fluorescent devices, light-emitting diodes, and liquid crystal displays and as photocatalysts, biosensors, and antibacterial drugs. Sulfide nanoparticles ~ 10 nm or smaller in size can be used as effective contrast agents in the study of biological tissues.

It can be expected that further development of the synthesis of sulfide nanoparticles with specified sizes and shapes will expand their application in optoelectronics, biology, and medicine.

The work was carried out under State Assignment No. 124020600013-9 at the Institute of Solid State Chemistry of the Ural Branch of the Russian Academy of Sciences.

References

1. Talapin D V et al. *Chem. Rev.* **110** 389 (2010)
2. Sadovnikov S I, Gusev A I, Rempel A A *Russ. Chem. Rev.* **85** 731 (2016); *Usp. Khim.* **85** 731 (2016)
3. Morozova N K, Kuznetsov V A *Sul'fid Tsinka. Poluchenie i Opticheskie Svoistva* (Zinc Sulfide. Production and Optical Properties) (Moscow: Nauka, 1987)
4. Fang X et al. *Prog. Mater. Sci.* **56** 175 (2011)
5. Wang X et al. *Crit. Rev. Solid State Mater. Sci.* **38** 57 (2013)
6. Kovalenko M V et al. *ACS Nano* **9** 1012 (2015)
7. Sadovnikov S I *Russ. Chem. Rev.* **88** 571 (2019); *Usp. Khim.* **88** 571 (2019)
8. Hullavarad N V, Hullavarad S S, Karulkar P C *J. Nanosci. Nanotechnol.* **8** 3272 (2008)
9. Kozhevnikova N S, Vorokh A S, Uritskaya A A *Russ. Chem. Rev.* **84** 225 (2015); *Usp. Khim.* **84** 225 (2015)
10. Cui C et al. *Nanoscale Res. Lett.* **10** 431 (2015)
11. Sadovnikov S I, Gusev A I *J. Mater. Chem. A* **5** 17676 (2017)
12. Sadovnikov S I, Rempel A A, Gusev A I *Russ. Chem. Rev.* **87** 303 (2018); *Usp. Khim.* **87** 303 (2018)
13. Sadovnikov S I, Rempel A A, Gusev A I *Nanostructured Lead, Cadmium, and Silver Sulfides: Structure, Nonstoichiometry and Properties* (Springer Ser. in Materials Science, Vol. 256) (Cham: Springer, 2018)
14. Lu C et al. *Adv. Eng. Mater.* **20** 1700940 (2018)
15. Xue J et al. *J. Mater. Chem. C* **7** 3988 (2019)
16. Sharma A et al. *J. Mater. Sci. Res. Rev.* **7** 42 (2021)
17. Yuan Y-J et al. *J. Mater. Chem. A* **6** 11606 (2018)
18. Nasir J A et al. *J. Mater. Chem. A* **8** 20752 (2020)
19. Sharma S et al. *Environ. Chem. Lett.* **19** 271 (2021)
20. Goel S, Chen F, Cai W *Small* **40** 631 (2014)
21. Wang L *RSC Adv.* **6** 82596 (2016)
22. Vasiliev R B, Dirin D N, Gaskov A M *Russ. Chem. Rev.* **80** 1139 (2011); *Usp. Khim.* **80** 1190 (2011)
23. Razumov V F *Phys. Usp.* **59** 1258 (2016); *Usp. Fiz. Nauk* **186** 1368 (2016)
24. Shuklov I A, Razumov V F *Russ. Chem. Rev.* **89** 379 (2020); *Usp. Khim.* **89** 379 (2020)
25. Nikolenko L M, Razumov V F *Russ. Chem. Rev.* **82** 429 (2013); *Usp. Khim.* **82** 429 (2013)
26. Gorbachev V V *Poluprovodnikovye Soedineniya* $A^{I}_{2}B^{VI}$ (Semiconductor $A^{I}_{2}B^{VI}$ Compounds) (Moscow: Metallurgiya, 1980)
27. Wang C et al. *Mater. Res. Bull.* **33** 1083 (1998)
28. Krylova V, Samuolaitienė L *Mater. Sci.* **19** (1) 10 (2013)
29. Fang X et al. *Chem. Commun.* (29) 3048 (2007)
30. Shen G et al. *J. Phys. Chem. C* **112** 12299 (2008)
31. Karashanova D et al. *Solid State Ionics* **171** 269 (2004)
32. Xu Z et al. *ACS Nano* **4** 2515 (2010)
33. Jiang P et al. *Biomaterials* **33** 5130 (2012)
34. Zhang W et al. *Solid State Ionics* **130** 111 (2000)
35. Yang H-Y et al. *Nanotechnology* **24** 055706 (2013)
36. Lv L, Wang H *Mater. Lett.* **121** 105 (2014)
37. Grocholl L, Wang J, Gillan E G *Mater. Res. Bull.* **38** 213 (2003)
38. Biswas S et al. *Cryst. Growth Des.* **8** 2171 (2008)
39. Bodo B, Singha R *Int. J. Sci. Res. Publ.* **6** 461 (2016)
40. Chen Z-G et al. *Adv. Funct. Mater.* **18** 3063 (2008)
41. Hedayati K, Zendehnam A, Hassanpour F *J. Nanostruct.* **6** 207 (2016) https://doi.org/10.7508/JNS.2016.03.005
42. Kryshtab T et al. *J. Lumin.* **129** 1677 (2009)
43. Gautam U K, Mukherjee B *Bull. Mater. Sci.* **29** 1 (2006)
44. Li S et al. *J. Colloid Interface Sci.* **330** 483 (2009)
45. Frueh A J (Jr.) *Z. Kristallogr.* **110** 136 (1958)
46. Van Aswegen J T S, Verleger H *Naturwissenschaften* **47** 131 (1960)
47. Smith P L, Martin J E *Phys. Lett.* **19** 541 (1965)
48. Sadanaga R, Ohmasa M, Morimoto N *Mineralog. J.* **4** 275 (1965) https://doi.org/10.2465/minerj1953.4.275
49. Ajibade P A, Botha N L *Results Phys.* **6** 581 (2016)
50. Kim B et al. *Environ. Sci. Technol.* **44** 7509 (2010)
51. Martínez-Castañón G A et al. *Mater. Lett.* **59** 529 (2005)
52. Liu Q et al. *Trans. Tianjin Univ.* **26** 273 (2020)

53. Awwad A M et al. *Chem. Int.* **6** 42 (2020) https://doi.org/10.5281/zenodo.3243157
54. Sousa D M et al. *ACS Omega* **5** 12877 (2020)
55. Ren Q et al. *ACS Omega* **6** 6361 (2021)
56. Prabhune V B, Shinde N S, Fulari V J *Appl. Surf. Sci.* **255** 1819 (2008)
57. Rempel A, Magerl A *Acta Cryst. A* **66** 479 (2010)
58. Vorokh A S, Rempel A A *Phys. Solid State* **49** 148 (2007); *Fiz. Tverd. Tela* **49** 143 (2007)
59. Rempel' A A et al. *J. Surf. Investig. X-Ray, Synchrotron Neutron Tech.* **5** 1028 (2011) https://doi.org/10.1134/S1027451011110152; *Poverkh. Rentgen. Sinkhrotron. Neitron. Issled.* (11) 8 (2011)
60. Chakrabarti D J, Laughlin D E *Bull. Alloy Phase Diagrams* **4** 254 (1983)
61. Evans H T (Jr.) *Nature Phys. Sci.* **232** 69 (1971)
62. Evans H T (Jr.) *Z. Kristallogr.* **150** 299 (1979)
63. Buerger M J, Wuensch B J *Science* **141** 276 (1963)
64. Barth T F W *Zentralbl. Mineral. Geol. Paläontologie A* **26** 284 (1926)
65. Morimoto N, Kullerud G *Am. Mineralogist* **48** 110 (1963)
66. Will G, Yinze E, Abdelrahman A R M *Eur. J. Mineral.* **14** 591 (2002)
67. Lukashev P et al. *Phys. Rev. B* **76** 195202 (2007)
68. Xu Q et al. *Appl. Phys. Lett.* **100** 061906 (2012)
69. Grønvold F, Westrum E F (Jr.) *J. Chem. Thermodyn.* **19** 1183 (1987)
70. Balapanov M Kh et al. *Inorg. Mater.* **43** 449 (2007); *Neorgan. Mater.* **43** 519 (2007)
71. Miller T A et al. *Nat. Commun.* **4** 1369 (2013)
72. Liang X *Appl. Phys. Lett.* **111** 133902 (2017)
73. Evans H T (Jr.), Konnert J A *Am. Mineralogist* **61** 996 (1976)
74. Fjellvag H et al. *Z. Kristallogr.* **184** 111 (1988)
75. Jiang X et al. *J. Mater. Chem.* **10** 2193 (2000)
76. Sharma R C, Chang Y A *Bull. Alloy Phase Diagrams* **7** 263 (1986)
77. Junod P *Helv. Phys. Acta* **32** 567 (1959)
78. Junod P et al. *Philos. Mag.* **36** 941 (1977)
79. Reye H, Schmalzried H *Z. Phys. Chem. Neue Folge* **128** 93 (1981)
80. Kashida S et al. *Sol. State Ionics* **158** 167 (2003)
81. Rau H *J. Phys. Chem. Solids* **35** 1553 (1974)
82. Bonnecaze G, Lichanot A, Gromb S *J. Phys. Chem. Solids* **39** 299 (1978)
83. Bonnecaze G, Lichanot A, Gromb S *J. Phys. Chem. Solids* **39** 813 (1978)
84. Reye H *Z. Phys. Chem. Neue Folge* **119** 251 (1980)
85. Sadanaga R, Sueno S *Mineralog. J.* **5** 124 (1967)
86. Sadovnikov S I, Gusev A I, Rempel A A *Superlattices Microstruct.* **83** 35 (2015)
87. Rahlfs P *Z. Phys. Chem. B* **31** 157 (1936)
88. Cava R J, Reidinger F, Wuensch B J *J. Solid State Chem.* **31** 69 (1980)
89. Blanton T et al. *Powder Diffraction* **26** 114 (2011)
90. Sadovnikov S I, Gusev A I, Rempel A A *Phys. Chem. Chem. Phys.* **17** 20495 (2015)
91. Frueh A J (Jr.) *Am. Mineralogist* **46** 654 (1961)
92. Sadovnikov S I, Gusev A I *J. Therm. Anal. Calorim.* **131** 1155 (2018)
93. Rempel A A, Sadovnikov S I, Klinser G, Sprengel W *JETP Lett.* **107** 4 (2018); *Pis'ma Zh. Eksp. Teor. Fiz.* **107** 6 (2018)
94. Sharma R C, Chang Y A *J. Phase Equilib.* **17** 261 (1996)
95. Kisi E H, Elcombe M M *Acta Cryst. C* **45** 1867 (1989)
96. Ves S et al. *Phys. Rev. B* **42** 9113 (1990)
97. Pius J J, Louis C N *Chem. Mater. Eng.* **4** 46 (2016)
98. Ono S, Kikegawa T *Phase Trans.* **91** 9 (2018)
99. Vorokh A S et al. *Dokl. Phys. Chem.* **470** 141 (2016); *Dokl. Ross. Akad. Nauk* **470** 417 (2016)
100. Vorokh A S, Rempel A A *Dokl. Phys.* **52** 200 (2007); *Dokl. Ross. Akad. Nauk* **413** 743 (2007)
101. Sharma R C, Chang Y A *J. Phase Equilib.* **17** 425 (1996)
102. Woodbury H H *J. Phys. Chem. Solids* **24** 881 (1963)
103. Ulrich F, Zachariasen W *Z. Kristallogr. A* **62** 260 (1925) https://doi.org/10.1524/zkri.1925.62.1.260
104. Traill R J, Boyle R W *Am. Mineralogist* **40** 555 (1955)
105. Razik N A *J. Mater. Sci. Lett.* **6** 1443 (1987)
106. Zelaya-Angel O et al. *Solid State Commun.* **104** 161 (1997)
107. Su B, Wei M, Choy K L *Mater. Lett.* **47** 83 (2001)
108. Metin H, Esen R *J. Cryst. Growth* **258** 141 (2003)
109. Maliki H El et al. *Appl. Surf. Sci.* **205** 65 (2003)
110. Wang W et al. *Mater. Lett.* **57** 2755 (2003)
111. Rempel A A et al. *Phys. Status Solidi B* **242** R61 (2005)
112. Potter R W (II), Barnes H L *Am. Mineralogist* **63** 1143 (1978)
113. Ohmiya T *J. Appl. Cryst.* **7** 396 (1974)
114. Bell A M T, Pattrick R A D, Vaughan D J *Mineralog. Mag.* **74** 85 (2010)
115. Ballirano P, Botticelli M, Maras A *Eur. J. Mineralogy* **25** 957 (2014)
116. Sharma R C, Chang Y A *Bull. Alloy Phase Diagrams* **7** 269 (1986)
117. Albers W et al. *J. Appl. Phys.* **32** 2220 (1961)
118. Albers W, Schol K *Philips Res. Rep.* **16** 329 (1961)
119. Wiedemeier H, Schnering H G *Z. Kristallogr.* **148** 295 (1978)
120. Wiedemeier H, Csillag F J *Z. Kristallogr.* **149** 17 (1979)
121. von Schnering H G, Wiedemeier H *Z. Kristallogr. Cryst. Mater.* **156** 143 (1981)
122. Chattopadhyay T, Pannetier J, von Schnering H G *J. Phys. Chem. Solids* **47** 879 (1986)
123. Bilenkii B F, Mikolaichuk A G, Freik D M *Phys. Status Solidi* **28** K5 (1968)
124. Burton L A, Walsh A *J. Phys. Chem. C* **116** 24262 (2012)
125. Rabkin A et al. *Nano Lett.* **15** 2174 (2015)
126. Abutbul R E et al. *CrystEngComm* **18** 5188 (2016)
127. Skelton J M et al. *APL Mater.* **5** 036101 (2017)
128. Popov I S et al. *Dokl. Phys. Chem.* **472** 23 (2017); *Dokl. Ross. Akad. Nauk* **472** 416 (2017)
129. Lin J C, Sharma R C, Chang Y *Bull. Alloy Phase Diagrams* **7** 374 (1986)
130. Noda Y et al. *Acta Cryst. B* **39** 312 (1983)
131. Qadri S B et al. *Appl. Phys. Lett.* **69** 2205 (1996)
132. Knorr K et al. *Eur. Phys. J. B* **31** 297 (2003)
133. Zhang B et al. *Nanotechnology* **14** 443 (2003)
134. Deng D et al. *J. Colloid Interface Sci.* **367** 234 (2012)
135. Yu Y, Zhang K, Sun S *Appl. Surf. Sci.* **258** 7181 (2012)
136. Sadovnikov S I et al. *Inorg. Mater.* **48** 21 (2012); *Neorgan. Mater.* **48** (1) 26 (2012)
137. Yu Y, Zhang K, Sun S *J. Mol. Struct.* **1031** 194 (2013)
138. Sadovnikov S I, Gusev A I *J. Alloys Compd.* **573** 65 (2013)
139. Rempel' A A *Phys. Usp.* **39** 31 (1996); *Usp. Fiz. Nauk* **166** 33 (1996)
140. Deng J, Zhao Z-Y *Mater. Res. Express* **6** 105513 (2019)
141. Sonawane P S et al. *J. Eng. Sci.* **11** (04) 1360 (2020) https://www.jespublication.com/login.php?id = 1232
142. Valeeva A A, Sadovnikov S I, Gusev A I *Nanomaterials* **12** 1668 (2022)
143. Baláž M et al. *Faraday Discuss.* **241** 367 (2023)
144. Strehlow W H, Cook E L *J. Phys. Chem. Ref. Data* **2** 163 (1973)
145. Gusev A I, Rempel A A *Nanocrystalline Materials* (Cambridge: Cambridge Intern. Science Publ., 2004)
146. Gusev A I *Phys. Usp.* **41** 49 (1998); *Usp. Fiz. Nauk* **168** 55 (1998)
147. Schaefer H-E *Nanoscience. The Science of the Small in Physics, Engineering, Chemistry, Biology and Medicine* (Heidelberg: Springer, 2010)
148. Ekimov A I, Onushchenko A A *JETP Lett.* **34** 345 (1981); *Pis'ma Zh. Eksp. Teor. Fiz.* **34** 363 (1981)
149. Kulakovskii V D, Lysenko V G, Timofeev V B *Sov. Phys. Usp.* **28** 735 (1985); *Usp. Fiz. Nauk* **147** 3 (1985)
150. Puls J, Rückmann I, Voigt J *Phys. Status Solidi B* **96** 641 (1979)
151. Hu Y Z et al. *Phys. Rev. Lett.* **64** 1805 (1990)
152. Klimov V I et al. *Science* **290** 314 (2000)
153. Murray C B, Norris D J, Bawendi M G *J. Am. Chem. Soc.* **115** 8706 (1993)
154. Kim S et al. *J. Am. Chem. Soc.* **125** 11466 (2003)
155. Steckel J S et al. *Angew. Chem.* **116** 2206 (2004)
156. Liu W et al. *J. Am. Chem. Soc.* **129** 14530 (2007)
157. Chen O et al. *Nature Mater.* **12** 445 (2013)
158. Ishihara T et al. *Surf. Sci.* **267** 323 (1992)
159. Moody G et al. *Phys. Status Solidi B* **250** 1753 (2013)
160. He Z et al. *ACS Nano* **10** 2176 (2016)
161. Yumoto G et al. *J. Phys. Chem. Lett.* **9** 2222 (2018)
162. Mondal S et al. *J. Phys. Chem. C* **122** 28497 (2018)
163. Hicks L D, Dresselhaus M S *Phys. Rev. B* **47** 12727 (1993)

164. Hicks L D, Dresselhaus M S *Phys. Rev. B* **47** 16631 (1993)
165. Saadeldin M et al. *Chinese Phys. B* **23** 046803 (2014)
166. Zhao Y et al. *J. Am. Chem. Soc.* **131** 4253 (2009)
167. Ramoin M et al. *C. R. Acad. Sci. B* **268** 1097 (1969)
168. He Y et al. *Jpn. J. Appl. Phys.* **41** 4630 (2002)
169. Liu G et al. *Thin Solid Films* **431–432** 477 (2003)
170. Sorokin G P, Papshev Yu M, Toush P *Sov. Phys. Solid State* **7** 1810 (1966); *Fiz. Tverd. Tela* **7** 2244 (1965)
171. Sobolev V V, Popov Yu V *Inorgan. Mater.* **5** 1285 (1969); *Izv. Akad. Nauk SSSR. Ser. Neorgan. Mater.* **5** 1513 (1969)
172. Puspitasari I, Gujar T P, Jung K-D *Mater. Sci. Eng. B* **140** 199 (2007)
173. Christy R S, Kumaran J T T *J. Non-Oxide Glass.* **6** 13 (2014)
174. Ghribi F et al. *Energy Proc.* **84** 197 (2015)
175. Ehrlich S H *J. Imaging Sci. Technol.* **37** 73 (1993)
176. Lin S et al. *J. Phys. Chem. C* **119** 867 (2015)
177. Lalanne P, Hugonin J P *Nature Phys.* **2** 551 (2006)
178. Abdulzadeh N N, Mursakulov N N, Ahmedsadeh R G, in *The 3rd Intern. Conf. on Technical and Physical Problems of Electrical Engineering, ICTPE-2006, May 29–31, 2006, Ankara, Turkey*, p. 819
179. Zhang Y et al. *J. Phys. Chem. C* **118** 4918 (2014)
180. Jackson K A, Schröter W (Eds) *Handbook of Semiconductor Technology* Vol. 2 *Processing of Semiconductors* (Weinheim: Wiley-VCH, 2000)
181. Kobyakov I B *Sov. Phys. Crystallogr.* **11** 369 (1966); *Kristallogr.* **11** 419 (1966)
182. Kobyakov I B, Pado G S *Sov. Phys. Solid State* **9** 1707 (1968); *Fiz. Tverd. Tela* **9** 2173 (1967)
183. Dan'kov I A, Kobyakov I B, Davydov S Yu *Sov. Phys. Solid State* **24** 2058 (1982); *Fiz. Tverd. Tela* **24** 3613 (1982)
184. Cardona M, Harbeke G *Phys. Rev.* **137** A1467 (1965)
185. Miklosz J C, Wheeler R G *Phys. Rev.* **153** 913 (1967)
186. Brus L E *J. Chem. Phys.* **80** 4403 (1984)
187. Ekimov A I, Onushchenko A A *JETP Lett.* **40** 1136 (1984); *Pis'ma Zh. Eksp. Teor. Fiz.* **40** 337 (1984)
188. Berger L I *Semiconductor Materials* (Boca Raton, FL: CRC Press, 1997)
189. Kobiakov I B *Solid State Commun.* **35** 305 (1980)
190. Ninomiya S, Adachi S *J. Appl. Phys.* **78** 1183 (1995)
191. Badalyan A M et al. *J. Struct. Chem.* **43** 556 (2002); *Zh. Strukt. Khim.* **43** 605 (2002)
192. Pässler R *Phys. Status Solidi B* **193** 135 (1996)
193. Zallen R et al. *Phys. Rev. B* **1** 4058 (1970)
194. Patel B K et al. *Appl. Phys. A* **86** 447 (2007)
195. Wichiansee W et al. *J. Mater. Chem.* **21** 7331 (2011)
196. Saini P K, Ahlawat D S, Singh D *Int. Res. J. Eng. Technol.* **4** 1080 (2017)
197. Siemsen K J, Riccius H D *Phys. Status Solidi* **37** 445 (1970)
198. Delin A *Phys. Rev. B* **65** 153205 (2002)
199. Zallen R, Slade M *Solid State Commun.* **8** 1291 (1970)
200. Dybko K et al. *Physica B* **256–258** 629 (1998)
201. Chamberlain J M, Merdan M *J. Phys. C* **10** L571 (1977)
202. Albers W, Haas C, van der Maesen F *J. Phys. Chem. Solids* **15** 306 (1960)
203. Albers W et al. *J. Appl. Phys.* **32** 2220 (1961)
204. Reddy N K, Devika M, Gopal E S R *Critical Rev. Solid State Mater. Sci.* **40** 359 (2015)
205. Tritsaris G A, Malone B D, Kaxiras E *J. Appl. Phys.* **113** 233507 (2013)
206. Elkorashy A M *Phys. Status Solidi B* **159** 903 (1990)
207. Greenaway D L, Nitsche R *J. Phys. Chem. Solids* **26** 1445 (1965)
208. Domingo G, Itoga R S, Kannewurf C R *Phys. Rev.* **143** 536 (1966)
209. Rau H *J. Phys. Chem. Solids* **27** 761 (1966)
210. Cuff K F et al., in *Proc. of the 7th Intern. Conf. on Physics of Semiconductors, Dunod, Paris, 1964*, p. 677
211. Ravich Y I, in *Lead Chalcogenides: Physics and Applications* (Ed. D Khokhlov) (New York: Taylor and Francis, 2003) p. 3
212. Zemmel J N, Jensen J D, Schoolar R B *Phys. Rev.* **140** A330 (1965)
213. Ravindra N M, Srivastava V K *Phys. Status Solidi A* **58** 311 (1980)
214. Zhang Y et al. *Phys. Rev. B* **80** 024304 (2009)
215. Schoolar R B, Dixon J R *Phys. Rev.* **137** A667 (1965)
216. Ukhanov Yu I *Opticheskie Svoistva Poluprovodnikov* (Optical Properties of Semiconductors) (Moscow: Nauka, 1977)
217. Kuznetsova Yu V et al. *J. Mol. Liq.* **371** 121084 (2023)
218. Sadovnikov S I, Kuznetsova Yu V, Rempel A A *Nano-Struct. Nano-Objects* **7** 81 (2016)
219. Popov I D et al. *J. Nanopart. Res.* **20** 78 (2018)
220. Popov I D et al. *J. Non-Cryst. Solids* **529** 119781 (2020)
221. Qian X-F et al. *Mater. Chem. Phys.* **68** 95 (2001)
222. Hmar J J L, Majumder T, Mondal S P *Thin Solid Films* **598** 243 (2016)
223. Onwudiwe D C et al. *Appl. Surf. Sci.* **290** 18 (2014)
224. Lu X et al. *Nanotechnology* **16** 2233 (2005)
225. Sadovnikov S I *Opt. Mater.* **141** 113928 (2023)
226. Xiao L et al. *AIP Adv.* **6** 085122 (2016)
227. Xie Y et al. *J. Am. Chem. Soc.* **135** 17630 (2013)
228. Shamraiz U, Hussain R A, Badshah A *J. Solid State Chem.* **238** 25 (2016)
229. Ku G et al. *ACS Nano* **6** 7489 (2012)
230. Fan Y et al. *Molecules* **24** 3776 (2019)
231. Jiang P et al. *Biomaterials* **33** 5130 (2012)
232. Smart R St C, Skinner W M, Gerson A R *Surf. Interface Anal.* **28** 101 (1999)
233. Wang C et al. *Small* **8** 3137 (2012)
234. Sadovnikov S I, Vovkotrub E G *J. Alloys Compd.* **766** 140 (2018)
235. Sun J et al. *J. Phys. Chem. Lett.* **5** 659 (2014)
236. Petrov Yu I *Fizika Malykh Chastits* (Physics of Small Particles) (Moscow: Nauka, 1982)
237. Sadovnikov S I, Gusev A I *J. Alloys Compd.* **610** 196 (2014)
238. Gusev A I, Sadovnikov S I *Thermochim. Acta* **660** 1 (2018)
239. Sadovnikov S I, Gusev A I, Rempel A A *Phys. Chem. Chem. Phys.* **17** 12466 (2015)
240. Bhattacharjee B et al. *Bull. Mater. Sci.* **25** 175 (2002)
241. Nanda J et al. *Chem. Mater.* **12** 1018 (2000)
242. Little R B et al. *J. Chem. Phys.* **114** 1813 (2001)
243. Li J B, Wang L-W *Phys. Rev. B* **72** 125325 (2005)
244. Zhang X et al. *Nanotechnology* **19** 305708 (2008)
245. Mir F A *J. Optoelectr. Biomed. Mater.* **2** 79 (2010)
246. Liem N Q et al. *Appl. Phys. Lett.* **75** 3974 (1999)
247. Gaponenko S V *Optical Properties of Semiconductor Nanocrystals* (Cambridge: Cambridge Univ. Press, 1998)
248. Babu K S et al. *Talanta* **66** 160 (2005)
249. Éfros Al L, Éfros A L *Sov. Phys. Semicond.* **16** 772 (1982); *Fiz. Tekh. Poluprovodn.* **16** 1209 (1982)
250. Rossetti R, Nakahara S, Brus L E *J. Chem. Phys.* **79** 1086 (1983)
251. Brus L E *J. Chem. Phys.* **79** 5566 (1983)
252. Rosetti R et al. *J. Chem. Phys.* **82** 552 (1985)
253. Brus L *J. Phys. Chem.* **90** 2555 (1986)
254. Ekimov A I, Efros Al L, Onushchenko A A *Solid State Commun.* **88** 947 (1993)
255. Banerjee R et al. *J. Phys. Condens. Matter* **12** 10647 (2000)
256. Yu W W, Peng X *Angew. Chem. Int. Ed.* **41** 2368 (2002)
257. Veamatahau A et al. *Phys. Chem. Chem. Phys.* **17** 2850 (2015)
258. Rempel' S V et al. *Phys. Solid State* **55** 624 (2013); *Fiz. Tverd. Tela* **55** 567 (2013)
259. Rempel' S V et al. *Phys. Solid State* **57** 1103 (2015); *Fiz. Tverd. Tela* **57** 1087 (2015)
260. Kuznetsova Yu V et al. *Fiz. Khim. Stekla* **42** 351 (2016)
261. Safardoust-Hojaghan H, Shakouri-Arani M, Salavati-Niasari M *Trans. Nonferrous Met. Soc. China* **26** 759 (2016)
262. Mahapatra A K, Dash A K *Physica E* **35** 9 (2006)
263. Azizian-Kalandaragh Y et al. *J. Nanopart. Res.* **15** 1388 (2013)
264. Mukherjee A, Mitra P *Mater. Sci. Poland* **33** 847 (2015)
265. Park H K et al. *Curr. Appl. Phys.* **15** 964 (2015)
266. Jana S et al. *Physica E* **40** 3121 (2008)
267. Chakraborty I, Moulik S P *J. Nanopart. Res.* **7** 237 (2005)
268. Moreels I et al. *Chem. Mater.* **19** 6101 (2007)
269. Huang Z, Beard M C *J. Am. Chem. Soc.* **144** 15855 (2022)
270. Zhang J et al. *J. Phys. Chem. C* **114** 11087 (2010)
271. Zhuang J et al. *J. Mater. Chem.* **13** 1853 (2003)
272. Zhou C et al. *J. Mater. Chem.* **21** 7393 (2011)
273. Zheng J J et al. *J. Phys. Chem. C* **114** 15331 (2010)

274. Jang E et al. *Adv. Mater.* **22** 3076 (2010)
275. Sadovnikov S I, Ishchenko A V, Weinstein I A *J. Alloys Compd.* **831** 154846 (2020)
276. Talapin D V et al. *Nano Lett.* **3** 1677 (2003)
277. Zheng W et al. *Adv. Func. Mater.* **26** 2648 (2016)
278. Chava R K, Do J Y, Kang M *J. Alloys Compd.* **727** 86 (2017)
279. Maskaeva L N et al. *Thin Solid Films* **461** 325 (2004)
280. Forostyanaya N A et al. *Chim. Techno Acta* **1** 98 (2014)
281. Sadovnikov S I *Int. J. Nanosci.* **18** 1940060 (2019)
282. Sadovnikov S I *Mendeleev Commun.* **29** 398 (2019)
283. Schou J et al. *Appl. Phys. A* **124** 78 (2018)
284. Tong H et al. *J. Phys. Chem. C* **111** 3893 (2007)
285. Hussein S K A et al. *Chalcogenide Lett.* **19** 363 (2022)
286. Thang B V et al. *Solar Energy Mater. Solar Cells* **250** 112042 (2023)
287. Ding C et al. *Adv. Mater.* **23** 2007768 (2021)
288. Sharma A et al. *Physica E* **151** 115730 (2023)
289. Singh R, Singh R R *Biointerface Res. Appl. Chem.* **13** 158 (2023)
290. Alwany A B et al. *Sci. Rep.* **13** 10314 (2023)
291. Gallardo-Benavente C et al. *Front. Microbiol.* **10** 1866 (2019)
292. Wang S et al. *ACS Omega* **6** 7139 (2021)
293. Widness J K et al. *J. Am. Chem. Soc.* **144** 12229 (2022)
294. Yang F et al. *J. Colloid Interface Sci.* **537** 422 (2019)
295. Wang J-C et al. *J. Inorg. Mater.* **34** 1156 (2019)
296. Luo X et al. *Appl. Phys. A* **127** 317 (2021)
297. Cheng Q et al. *Small* **19** 2302188 (2023)
298. Ngo T T et al. *Nanoscale Adv.* **1** 4109 (2019)
299. Sukharevska N et al. *ACS Appl. Mater. Interfaces* **13** 5195 (2021)